



Sensitivity of tidal range assessments to harmonic constituents and analysis timeframe

Konstantinos Pappas^{a,*}, Lucas Mackie^b, Ilias Zilakos^c, Adriaan Hendrik van der Weijde^d, Athanasios Angeloudis^a

^a Institute for Infrastructure and the Environment, The University of Edinburgh, Edinburgh, UK

^b Department of Earth Science & Engineering, Imperial College London, London, UK

^c Tidetec AS, Oslo, Norway

^d The Netherlands Organization for Applied Scientific Research (TNO), The Hague, The Netherlands

ARTICLE INFO

Keywords:

Tidal range
Tidal range energy
Tide variability
Energy assessment
Resource assessment

ABSTRACT

Tides exhibit variability over time. This study proposes a methodology for selecting a representative timeframe for tidal range energy analyses, when constrained to a typical, short-term, lunar month-long period. We explore how the selection of particular timeframes skews findings of energy assessments, especially for cross-comparisons across studies. This exercise relies on metrics assessing the magnitude and variability of a tidal signal relative to longer-term nodal cycle quantities. Results based on UK tide gauges highlight that tide characteristics exhibit significant variations temporally within a lunar month. Relative to quantities of tidal elevation standard deviation or average potential energy, values can vary by 15% and 30% respectively. For each lunar month, interquartile range values for tidal height and energy can deviate by 45% from the mean. Spatially, we observe a satisfactory correlation only once sufficient constituents are considered. In that case, a representative timeframe can be identified for comparative tidal range scheme assessments within the same tidal system. In contrast, timeframes with high tidal variability distort individual project performance, particularly under fixed operation. The methodology, if integrated to marine energy resource and environmental impact assessments, would deliver marine power generation insights over a project lifetime that enable robust design comparisons across sites.

1. Introduction

Tides are very long waves modulated by wave transformation effects over complex bathymetry. As such, they can exhibit an energy density which is significantly spatially variable. As tidal elevations or velocities amplify above certain thresholds, they can be perceived as an attractive energy source, particularly given their predictability. Marine energy developments, therefore, could contribute significantly towards a net zero energy system [1]. Generally, tidal energy technologies can be classified into ‘range’ or ‘stream’ variants. In the former, the objective is to harness the tide’s potential energy, typically in sites of amplified resonance [2]. In the latter, the target is the conversion of kinetic energy that is present within high velocity currents driven through tidal streaming or hydraulic gradients [3]. In this study, we are motivated by efforts to harness potential energy through tidal range structures proposed at coastal regions of sufficient resource and depth for siting hydro-turbines. Their operation principle entails periodically exploiting a head difference between elevations of water bodies across

a tidal barrier. This head difference drives the flow through low head hydro-turbines, generating electricity [4].

Assessment of tidal energy technologies, including optimisation and impact quantification of specific engineering designs, relies on numerical modelling of their operation in time [5,6]. Hydrodynamic modelling is an integral component of such assessments. However, factors including bathymetry, open boundary, atmospheric forcing, spatial resolution are potential sources of sea surface height and other prediction uncertainties [7]. In particular, tidal forcing at model boundary conditions is typically informed by a limited set of constituents that varies between studies (Table 1). Furthermore, simulations are typically conducted over short timeframes (i.e. in the order of weeks or months) given computational and practical constraints when running hydrodynamic models [8,9]. When using hydrodynamic modelling that introduces tangible computational constraints, these assessments tend to simulate finite periods in the order of a lunar month (i.e., ≈ 29.53 days [10,11]). As such a period includes two spring-neap cycles, this is a sufficient

* Corresponding author.

E-mail address: k.pappas@ed.ac.uk (K. Pappas).

<https://doi.org/10.1016/j.renene.2023.01.062>

Received 27 September 2022; Received in revised form 22 December 2022; Accepted 15 January 2023

Available online 18 January 2023

0960-1481/© 2023 The Authors. Published by Elsevier Ltd. This is an open access article under the CC BY license (<http://creativecommons.org/licenses/by/4.0/>).

Nomenclature

$\mathcal{E}_{M_{k,j}}$	array of theoretical tidal range energy entries E_i within $M_{k,j}$
$\mathcal{G}_{M_{k,j}}$	array of extractable tidal range energy entries $E_{0D,i}$ within $M_{k,j}$
$\mathcal{R}_{M_{k,j}}$	array of tidal range entries R_i within $M_{k,j}$
\overline{PE}	temporally averaged wave potential energy per unit surface area (Wh/m ²)
\overline{PE}_k	temporally averaged wave potential energy per unit surface area for wave elevation represented by the k th constituent (Wh/m ²)
\overline{R}	mean annual tidal range (m)
\bar{z}	height to the water column centre of mass (m)
$\{V_0 + u\}_i$	equilibrium argument for the i th constituent at time zero
A_s	tidal range structure impounded surface area (km ²)
C	predicted capacity (W)
C_F	capacity factor
$D_{m,n}$	Kolmogorov–Smirnov two-sample test statistic
E_i	available tidal range energy per unit surface area for a tidal range R_i (Wh/m ²)
E_{max}	theoretically available potential energy for a tidal range structure per unit surface area (Wh/m ²)
F	form factor
f_i	node factor of the i th constituent
$F_{\mathcal{X},m}$	cumulative distribution function of m -size sample \mathcal{X}
g	gravitational acceleration (m/s ²)
h	water surface depth to the datum (m)
H_{m_0}	significant wave height (m)
IQR	interquartile range
N	nodal cycle
N_s	number of sluice gates
N_t	number of turbines
P_{50}	median
P_{max}	turbine rated power (W)
R_i	tide range over the i th transition (m)
W_1	1-Wasserstein distance
$M_{k,j}$	j th lunar month corresponding to a tidal segment reconstructed using k constituents
MAE	mean absolute error
NRMSE	normalised root mean square error
R^2	coefficient of determination
RMSE	root mean square error
t	time (s)

Greek symbols

α_i	mean amplitude of the i th constituent (m)
η	water elevation of tidal signal (m)
η_e	expected generation efficiency factor
$\eta_{g,i}$	generation efficiency factor over the i th transition
η_i	predicted water elevation (m)
$\hat{\eta}_i$	observed water elevations (m)
μ	mean of (discrete) observed water elevations (m)

μ_η	mean of (continuous) predicted water elevations (m)
ω_i	angular speed of the i th constituent (rad/h)
$\bar{\eta}_g$	lunar-monthly generation efficiency factor
ϕ_i	phase lag of the i th constituent (rad)
ρ	water density (kg/m ³)

Subscripts

D	$D_{m,n}$ metric
k	number of constituents
r	approach of current research
W	W_1 metric

regarding performance and project feasibility. However, the selection of appropriate simulation periods and the essential constituents to support modelling that leads to robust conclusions is not currently based on concrete, evidence-based guidance.

This study aims to address this gap. We investigate the significance of (a) the *tide harmonic constituent set* used in tidal elevation signal reconstruction, and (b) the specific *date interval*, i.e. timeframe, selected for robust tidal range energy and impact assessments. This sets our research question as the identification of a representative tidal signal spanning a lunar-monthly period in terms of its variation of tidal range, its potential energy, and the extractable tidal range energy relative to a nodal tidal cycle [12].

2. Background

There are numerous studies associated with tidal range energy (Table 1), but little is mentioned on the rationale behind performing simulations over a certain timeframe [13], or the determination of average tide conditions. Usually, the simulation timeframe of hydrodynamic modelling studies is based on the presence of validation data. More generally, the significance of having sufficiently long period signals is highlighted in Haigh et al. [14]. They investigate the global contribution of the 18.61 year nodal cycle and the 8.85 year cycle of lunar perigee on extreme tidal levels. In our study, we instead focus on signals with a duration of a lunar month due to a range of practical engineering constraints. With such a short interval, the uncertainty associated with energy quantification increases, partially due to the quadratic relationship between the tidal range and potential energy (see Eq. (8)). We present below examples from studies that motivate this research.

Burrows et al. [9] considered the conjunctive operation of five major tidal barrages on the west coast of the UK. The addition of three constituents aside from the principal M_2 and S_2 (which were used in their analysis), provide noticeable changes to the energy source, indicating that these should be considered for more accurate resource assessments. It should be noted that in the simple case of solely using M_2 and S_2 over a lunar month, the tidal signal becomes periodic. Complexity arises when additional constituents that take longer to resolve are introduced over a constrained analysis timeframe.

Mejia-Olivares et al. [15] explored the tidal range energy resource of the Gulf of California, Mexico, and showed that when reducing the number of constituents from 13 to the principal M_2 and S_2 the maximum tidal range from 8 to 5 m and the mean tidal range reduces from 5 to 4 m in the northern part of the Gulf. In addition, the potential annual energy yield ranges from 20 to 50 kWh/m² across different locations when considering all model constituents, while using only M_2 and S_2 constituents returns on average –10 to –13 kWh/m² lower resource.

Cornett et al. [16] investigated changes in tidal hydrodynamics at the Bay of Fundy, Canada, in the presence of tidal range energy lagoons.

duration to discern the principal lunar and solar tide constituents (M_2 , S_2), even though more constituents are often used within the analysis. Results from these studies are in turn extrapolated to draw conclusions

Table 1

Examples of modelling studies related to tidal range resource. Columns include percentage differences of averaged potential energy \overline{PE} , tidal range energy \mathcal{E} variability (IQR), and rating scores of study periods relative to Section 3.5. Tidal signals were reconstructed using the 12 leading constituents and the signal duration was adjusted to the reported timeframe Δt .

Studies	Cons.	Simulation start date	Timeframe Δt (M) ^a	$\frac{\Delta \overline{PE}}{\overline{PE}(N,12)}$	$\frac{\Delta IQR(\mathcal{E})}{IQR(\mathcal{E}(N,12))}$	Rating **			Location	Lat, Lon (°N, °E)
				(%)	(%)	RS_r	RS_D	RS_W		
UK Studies										
Aggidis and Benzon [20] ^a , Aggidis and Feather [21] ^b , Petley and Aggidis [22] ^b	4 ^{a3}	–	12.4	–	–	–	–	–		
Angeloudis and Falconer [23] ^c	–	06/03/2005	1	3.1	42.3	0.47	0.51	0.22		
Angeloudis et al. [4] ^{c,d} , Baker et al. [24] ^e	8 ^{a4}	06/05/2003	1	–3.9	–23.3	0.61	0.47	0.67		
Angeloudis et al. [25] ^b	8 ^{a5}	06/05/2003	3	–4.4	–19.7	0.47	0.32	0.42		
Angeloudis [26] ^b	9 ^{a5}	06/05/2003	2	–5.3	–25.7	0.44	0.15	0.39		
Burrows et al. [9,27] ^a	2, 5 ^{a6}	–	1	–	–	–	–	–		
Mackie et al. [28] ^b	8 ^{a4}	01/01/2018	1	–2	–37.3	0.62	0.40	0.43		
Mackie et al. [18] ^e	8 ^{a4}	14/01/2002	2	2.2	–11.2	0.77	0.86	0.80	Avonmouth, UK	(51.51, –2.71)
Xue et al. [29] ^b	–	17/01/2012	0.5	–3.2	–8.8	0.88	0.74	0.83		
Yates et al. [30] ^a	2 ^{a7}	–	–	–	–	–	–	–		
Xia et al. [31] ^a	–	10/03/2003	0.5	10.1	73.5	0.31	0.55	0.28		
Xia et al. [32] ^e	–	05/05/2003	0.25	–32.3	–45	0.48	0.31	0.57		
Bray et al. [33] ^e , Zhou et al. [34] ^e	–	01/03/2005	0.5	17.6	33.3	0.28	0.63	0.35		
Čož et al. [35] ^e	–	19/01/2012	0.5	–5.7	–4.6	0.82	0.74	0.89		
Gao and Adcock [36] ^e	1 ^{a1}	–	–	–	–	–	–	–		
Idier et al. [37] ^f	14 ^{a7}	01/01/2009	12.4	0.02	6.83	0.67	0.43	0.27		
Non-UK Studies										
Huang et al. [38] ^e	8 ^{a4}	17/06/2018	1.7	–5.2	–25.8	0.32	0.38	0.31	Sandy Hook, USA	(40.47, –74.01)
Lee et al. [39] ^g	5 ^{a8}	01/15/2003	1.9	3.84	–12.57	0.39	0.33	0.31	Annapolis, USA	(38.96, –76.45)
Neill et al. [40] ^a	5 ^{a8}	01/01/2019	12.4	–1.05	–6.8	0.56	0.21	0.26	King Sound, AU	(–16.89, 123.65)
Cornett et al. [16] ^f	10 ^{a9}	26/07/2009	0.5	–12.11	–65.90	0.54	0.57	0.54	Five Islands, CA	(45.39, –64.06)
Mejia-Olivares et al. [15] ^a	13 ^{a11}	1/12/2015	12.4	–1.25	–1.57	0.61	0.53	0.52	Santa Clara, MX	(31.49, –114.48)
Park [41] ^e	8 ^{a4}	–	1	–	–	–	–	–	Sihwa Lake, KOR	(37.32, 126.61)
Bae et al. [42] ^{c,d}	21 ^{a12}	01/02/2009	1	3.9	14.57	0.62	0.41	0.55	Sihwa Lake, KOR	(37.32, 126.61)
Rtimi et al. [43] ^e	11 ^{a10}	15/08/2019	0.5	–12.10	–25.25	0.70	0.42	0.60	La Rance, FR	(48.62, –2.02)

^a Energy resource assessment, ^b Operation optimisation, ^c Tidal energy operation modelling, ^d General coastal modelling, ^e Environmental/Hydrodynamic impacts, ^f Sea level rise. ^g Approximate values are used based on content with M denoting lunar months. $\dagger \Delta \overline{PE} = \overline{PE}(\Delta t, 12) - \overline{PE}(N, 12)$, $\Delta IQR(\mathcal{E}) = IQR(\mathcal{E})(\Delta t, 12) - IQR(\mathcal{E})(N, 12)$. **Constituents sets:** ^{a1} M_2 , ^{a2} $[M_2, S_2]$, ^{a3} $[M_2, S_2, K_1, S_1]$, ^{a4} $[M_2, S_2, N_2, K_1, Q_1, O_1, P_1, K_2]$, ^{a5} $[M_2, S_2, N_2, K_1, Q_1, O_1, P_1, K_2, M_4]$, ^{a6} $[M_2, S_2]$ and $[M_2, S_2, N_2, O_1, K_1]$ for 0-D and 2-D simulations respectively, ^{a7} $[M_1, M_m, M_{sqm}, M_{tm}, O_1, P_1, Q_1, K_1, M_2, K_2, 2N_2, N_2, S_2, M_4]$, ^{a8} $[M_2, S_2, N_2, K_1, O_1]$, ^{a9} $[M_2, S_2, N_2, K_1, Q_1, K_2, L_2, 2N_2, \nu_2, M_4]$, ^{a10} $[M_2, S_2, N_2, K_2, K_1, O_1, P_1, Q_1, M_4, MS_4, MN_4]$, ^{a11} $[M_2, S_2, N_2, K_2, K_1, O_1, P_1, Q_1, M_4, MS_4, MN_4, M_1, M_m]$, ^{a12} $[M_2, S_2, K_1, O_1, N_2, K_2, P_1, Q_1, M_1, J_1, OO_1, 2N_2, \mu_2, \nu_2, L_2, T_2, M_f, M_{sf}, M_m, S_{sa}, S_a]$.

Ten constituents were considered to reconstruct sea surface elevations in the open ocean boundary. Cornett et al. [16] acknowledged that the addition of constituents beyond M_2 provides more realistic predictions and more accurate assessments. The duration of the simulations was limited to the same 15 day-period (\approx half a lunar month), arguing that the spring and neap tides contained in this interval were very close to long-term average conditions. However, a definition of what constitutes such average conditions was not reported.

Xue et al. [17] reported that the difference between the maximum and minimum energy outputs of tidal range structures over spring-neap cycles can be in the order of 25%. In turn, the study defined a representative period for annual generation estimation as the cycle with the smallest deviation from the time-averaged annual output. However, this approach solely focuses on the aggregate energy output and does not provide insight into how representative the tidal elevation signal can be relative to long-term variability.

More recently, Mackie et al. [18] made use of representative tidal level definitions from the National Tidal and Sea Level Facility [19] (e.g. Mean high/low water springs/neaps) across several locations around the UK to identify an appropriate interval to assess multiple tidal range designs at various locations. Again, this identification relies on a handful of discrete values with limited insight to the variations over spring-neap cycles, motivating further research.

For completeness, relevant UK-based and international studies that report on the number of constituents and simulation timeframes as part of tidal range and/or energy assessments, are summarised in Table 1.

3. Methodology

The aim of the study is to present a methodology to determine representative tide conditions that can be applied for a more robust tidal resource and power plant operation performance characterisation in the UK and, by extension, to other coastal regions of tidal energy interest internationally. The approach we adopt is as follows:

1. We employ harmonic analysis to extract the most influential constituents across tide gauge sites along the UK coast, where substantial observational records are available. In turn, tidal signals are reconstructed based on different constituent sets and applied as input in the analysis that follows.
2. We quantify tidal wave quantities of interest (tidal range R , significant wave height H_{m0} , tidal range energy E and average potential energy \overline{PE} - see Section 3.4) as metrics to evaluate periods used for the analysis.
3. We perform simulations of tidal power plant operation, by applying a 0-D modelling approach, to investigate the link between the available resource magnitude and its variability to the practically extractable energy E_{0D} .
4. We assess three different strategies to rank candidate lunar months within the nodal cycle; namely, the Kolmogorov–Smirnov statistic ($K-S$), Wasserstein distance (W_1) and a custom method based on the tidal quantities we prioritise as representative for magnitude and variability. These are used as metrics to provide a

rating for a particular timeframe in terms of how representative it is.

3.1. Tidal signal reconstruction

Tides are a regular and predictable phenomenon in the form of very long waves that arise from the gravitational forces between the Earth, Moon and Sun. The periodic motions in this system determine the various frequencies, and therefore patterns, at which tidal waves occur. Using harmonic analysis these patterns can be broken down to their tidal constituents, represented by an amplitude and a phase [44]. The water elevation of any tidal signal at any location and at arbitrary time can be reconstructed as [44]:

$$\eta(t) = h + \sum_{i=1}^k f_i \alpha_i \cos(\omega_i t + \{V_0 + u\}_i - \phi_i) \quad (1)$$

where h is the mean surface level above the datum, f_i is a node factor to account for the effect of the nodal cycle on the amplitude of constituent i , $\{V_0 + u\}_i$ is an equilibrium argument for constituent i at time zero, α_i is the constituent's mean amplitude of the nodal cycle at the location, and ω_i , ϕ_i the angular speed and the phase lag of the constituent at the location behind the corresponding constituent at Greenwich.

In this study harmonic analysis is conducted using the Python package *uptide* [45] to reconstruct tidal signals at 46 tide gauge stations across the UK as in Fig. 2. Harmonic analysis determines the amplitude and phase of tidal frequencies using a Least Squares Regression approach [45]. Tide gauge data provided by the British Oceanographic Data Centre (BODC) [46] are utilised in the reconstruction process. The start date has been chosen arbitrarily as 01/01/2002 00:00:00. The duration of the recorded time series excluding invalid values in the reconstruction process varies from 2.2 to 16.3 years (depending on the availability of recordings as displayed in Fig. 2). The recordings at tide gauge locations can be intermittent and certainly do not span a sufficient duration to cover a nodal cycle. As such, tidal elevation signal reconstruction becomes essential to create continuous elevation signals over the entire nodal cycle. We compare these against observed water levels at tide gauge locations. An example of these time-series including a varying number of leading constituents is presented in Fig. 1, where the tidal range R_i recorded by the i th transition from high water to low water and vice versa is annotated.

Table 2 presents an example of the amplitude (α) and phase (ϕ) of the most influential constituents at two locations, namely Avonmouth and Llandudno (i.e. Points 1 and 11 of Fig. 2). Constituents are perceived as influential assuming they are of appropriate amplitude and period to affect tidal conditions within a lunar month. It is instructive to introduce a 'participation percentage quantity', $\alpha_i / \sum \alpha$, relative to the aggregate amplitude of known constituents as an indication of influence to the tidal signal over the timescales considered. As expected for UK waters, on all tide gauge locations, the principal semidiurnal constituents M_2 , S_2 and N_2 are prevailing in this order. Aside from the principal semi-diurnal constituents, the contribution of the remaining constituents varies in rank relative to their participation percentage. For instance, in Avonmouth, where the estuary becomes narrower and the basin depth shallower, shallow-water overtide constituents become more influential compared to other locations, e.g. Llandudno, where the stream-wise channel is less constricted. Indicatively, the MS_4 participation factor in Avonmouth is almost twice that recorded at the Llandudno station.

3.2. Statistical parameters

Four error metrics are used to statistically evaluate the accuracy of reconstruction; the Root Mean Square error (RMSE), the Normalised

Root Mean Square Error (NRMSE), the Mean Absolute Error (MAE) and the coefficient of determination (R^2), defined as

$$\text{RMSE} = \sqrt{\frac{\sum_{i=1}^n (\hat{\eta}_i - \eta_i)^2}{n}} \quad (2)$$

$$\text{NRMSE} = \frac{\sqrt{\sum_{i=1}^n (\hat{\eta}_i - \eta_i)^2}}{\sqrt{\sum_{i=1}^n (\eta_i - \mu)^2}} \quad (3)$$

$$\text{MAE} = \frac{\sum_{i=1}^n |\hat{\eta}_i - \eta_i|}{n} \quad (4)$$

and

$$R^2 = 1 - \frac{\sum_{i=1}^n (\hat{\eta}_i - \eta_i)^2}{\sum_{i=1}^n (\eta_i - \mu)^2}, \quad (5)$$

where n is the length of data set, μ is the mean of observed water elevations, $\hat{\eta}_i$ the observed values and η_i the predicted ones. Notably, NRMSE is preferred to RMSE in order to provide a fair comparison given the variation of the tidal range magnitude across tide gauge stations.

3.3. Representative lunar month definitions

In setting out this study, we consider that a nodal cycle N of 18.6134 years contains 13137 M_2 periods, with $T = 12.42$ h. A lunar month M of 29.53 days contains 57 M_2 tidal cycles. The approach taken here assumes that a lunar month segment can start at the beginning of any M_2 periods forming the nodal cycle, and thus we consider 13137 lunar cycles. Fig. 3a illustrates how these quantities are used as arguments in defining the water elevation time series interval $\eta(\Delta t, k, j)$ and the notation for representative lunar months as elaborated in the following sections.

3.4. Target representative quantities

As tides are very long waves, we adopt some widely used coastal wave statistics. For example, tidal range itself corresponds to wave height, and the tide elevation standard deviation from MWL would refer to the significant wave height H_{m_0} .

3.4.1. Tidal range

3.4.1.1. Tidal range magnitude R . The tidal range magnitude R_i is defined as the difference between high and low water in the i th transition from elevation peaks to troughs or vice versa (Fig. 1a). As in Fig. 1b, tide signals of multiple constituents are not sinusoidal, and they vary over short- and long-term timescales according to each constituent's amplitude and phase. If we consider the distribution of R_i per lunar month, a relatively short-term period of 57 M_2 cycles, it becomes clear that the distribution is non-Gaussian (Fig. 4). However, by observing the same distribution over the significantly longer nodal cycle (e.g. Fig. 4d for 12 constituents) a quasi-normal distribution emerges as per the Central Limit Theorem. Given our constraint to a finite period, we adopt non-parametric approaches (see Section 3.5) to compare lunar-monthly to nodal quantities. We denote as $\bar{R}(M, k, j)$, arrays containing the tidal range R_i of every transition i within the j th lunar month M , reconstructed using k constituents. Similarly, $\bar{R}(N, k, 1)$ is the set of R_i values over the nodal cycle N .

3.4.1.2. Significant wave height H_{m_0} . The set of R_i is a discrete set of values relying on the peaks and troughs of the signal; however, this can omit information regarding the shape of the wave. In acknowledging this, the significant wave height H_{m_0} is considered based on its common application to coastal wave characterisation as in Defne et al. [48]. H_{m_0} is defined using the standard deviation σ_η from mean water level as:

$$H_{m_0} = 4\sigma_\eta \quad (6)$$

Table 2

Constituent information extracted from tide gauge records of BODC [46], for Avonmouth and Llandudno, UK. $\alpha/\Sigma\alpha$ and $\overline{PE}/\Sigma\overline{PE}$ are percentages of related variables (amplitude and potential energy) that indicate the overall contribution to the aggregate amplitude ($\Sigma\alpha$) and average energy flux ($\Sigma\overline{PE}$) for $k = 16$.

Constituents	Origin [44]	T (h)	Avonmouth, UK				Llandudno, UK			
			α_i (m)	$\alpha_i/\Sigma\alpha$ (%)	$\overline{PE}_i/\Sigma\overline{PE}$ (%)	ϕ_i (°)	α_i (m)	$\alpha_i/\Sigma\alpha$ (%)	$\overline{PE}_i/\Sigma\overline{PE}$ (%)	ϕ_i (°)
Diurnal:										
K_1	Luni-solar	23.93	0.07	0.8	0.0	132	0.12	2.3	0.2	173
O_1	Lunar	25.81	0.07	0.8	0.0	14	0.11	2.1	0.1	49
Semidiurnal:										
M_2	Lunar	12.42	4.29	46.0	83.3	197	2.69	51.8	86.2	307
S_2	Solar	12.00	1.53	16.4	10.5	259	0.87	16.8	9.0	351
N_2	Lunar	12.66	0.77	8.3	2.7	183	0.52	10.0	3.2	284
K_2	Luni-solar	11.97	0.42	4.5	0.9	236	0.24	4.6	0.7	328
L_2	Lunar	12.19	0.30	3.2	0.4	181	0.12	2.3	0.2	328
T_2	Solar	29.96	0.10	1.1	0.0	253	0.05	1.0	0.0	344
λ_2	Lunar	12.22	0.16	1.7	0.1	176	0.05	1.0	0.0	319
$2N_2$	Lunar	12.90	0.10	1.1	0.0	171	0.07	1.4	0.1	260
μ_2	Lunar	12.87	0.51	5.5	1.1	253	0.01	0.2	0.0	77
ν_2	Lunar	12.63	0.19	2.0	0.2	146	0.12	2.3	0.2	286
$2SM_2$	Shallow	11.61	0.15	1.6	0.1	80	0.03	0.6	0.0	222
Higher-Order:										
MS_4	Shallow	6.10	0.24	2.6	0.2	17	0.07	1.4	0.1	230
M_4	Shallow	6.21	0.26	2.8	0.3	343	0.11	2.1	0.2	180
$2MS_6$	Shallow	4.09	0.16	1.7	0.1	320	0.01	0.0	0.0	44

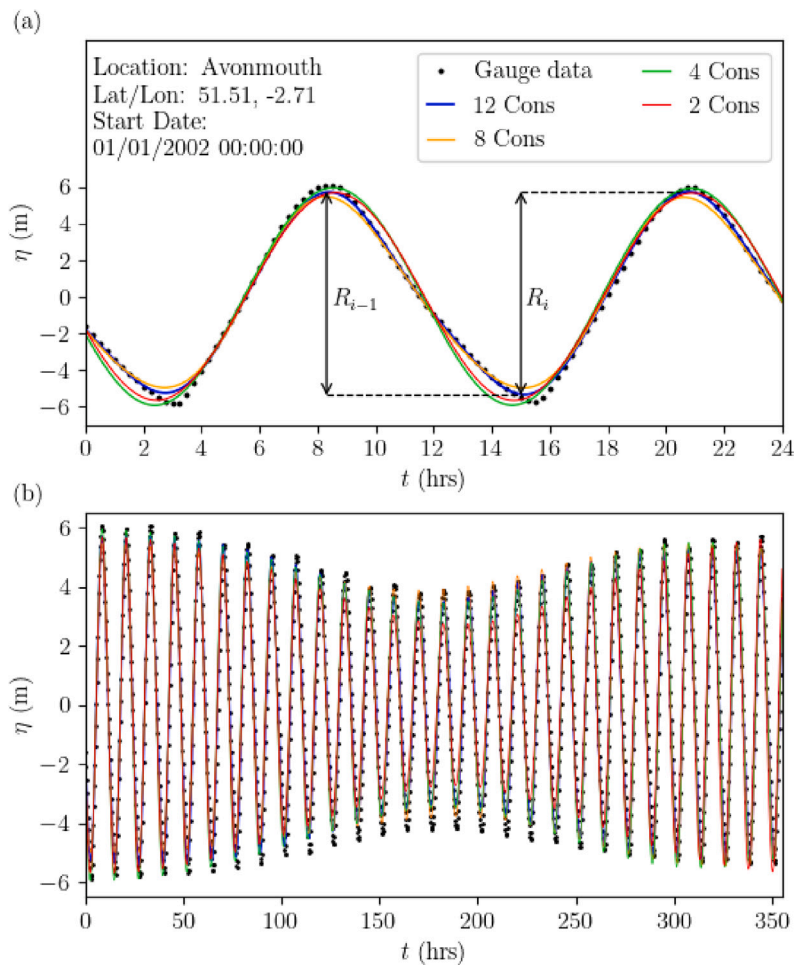


Fig. 1. Elevation-time reconstructed signals at Avonmouth, Severn Estuary, UK vs recorded data. Indicatively, R_i is the predicted tidal range (in this case annotated for the 12 leading constituents signal) of the i th transition from low to high waters and vice versa. (a) Over a day. (b) Over a spring-neap period of 14.76 days.

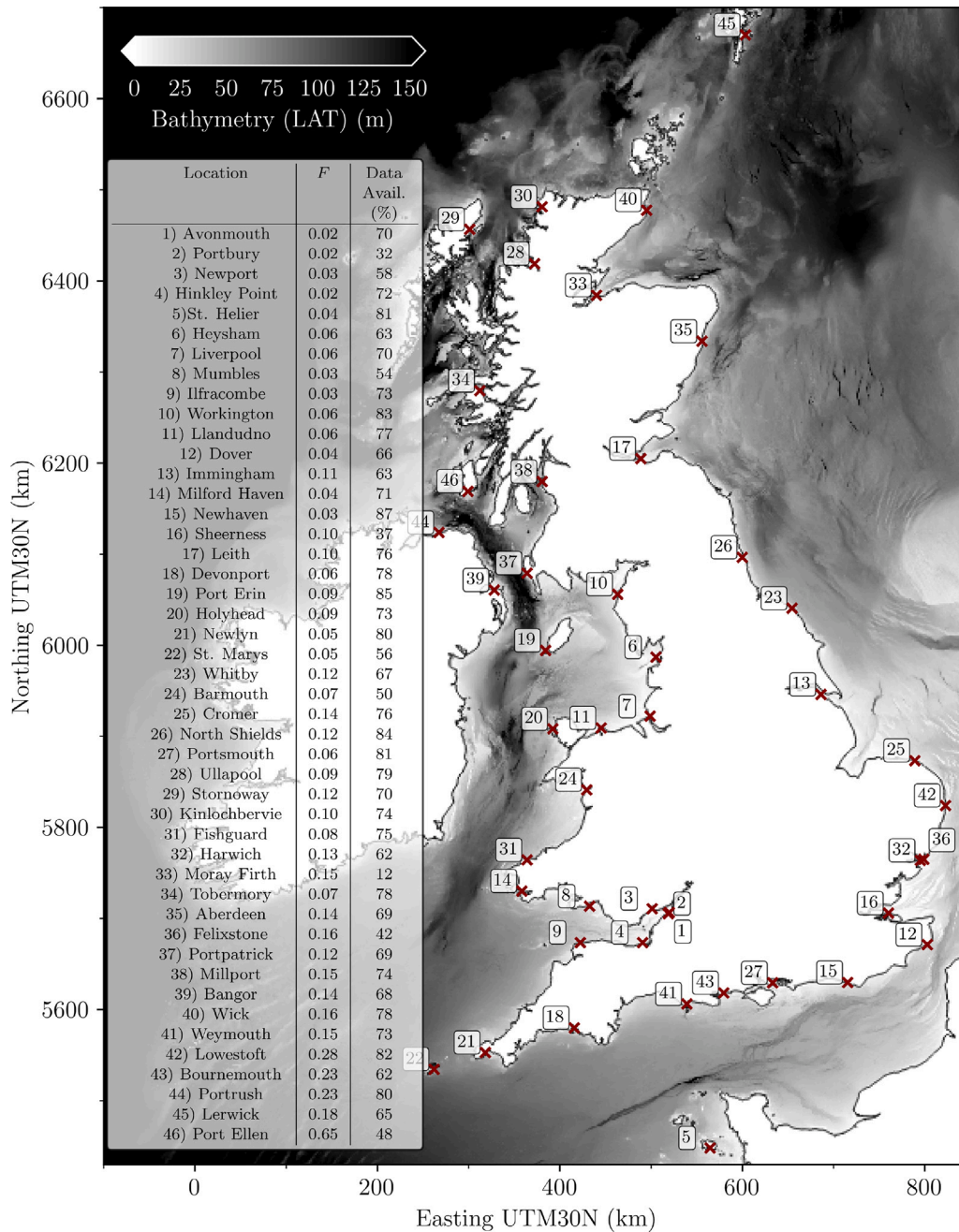


Fig. 2. Map of tide gauge monitor points utilised for the analysis alongside the corresponding form factors for classification of tides. Bathymetry (m) in 1/3600° resolution from the GEBCO [47] dataset. Tide gauge sites are ordered based on the magnitude of their aggregated amplitude $\Sigma\alpha$. The form factor $F = \frac{\alpha_{K_1+O_1}}{\alpha_{M_2} + \alpha_{S_2}}$, where α_i , the amplitudes of harmonic constituents for $i \in \{M_2, S_2, K_1, O_1\}$ is indicated. For $F < 0.25$ tides are classified as semidiurnal; while, for $0.5 < F < 1.5$ as mixed-mainly semidiurnal.

where

$$\sigma_\eta = \sqrt{\int_{-\infty}^{\infty} (\eta - \mu_\eta)^2 f(\eta) d\eta}, \tag{7}$$

so that $\mu_\eta = \int_{-\infty}^{\infty} \eta f(\eta) d\eta$ is the mean and $f(\eta)$ is the probability density function of the tidal signal segment $\eta(\Delta t, k, j)$, with arguments $\Delta t, k, j$ as defined in Fig. 3.

3.4.2. Tidal range energy

In this section, we consider the ambient and extractable energy acknowledging that the latter would be affected by turbine efficiency considerations over variable tidal conditions.

3.4.2.1. Available tidal range energy E . Tidal elevations can be used as an input to determine the potential energy that can be targeted through the operation of a tidal range power plant [49]. The theoretically available potential energy per unit surface area contained in a tidal range structure over a tidal range R_i , neglecting any form of losses can be quantified as [50]:

$$E_i = \frac{1}{2} \rho g R_i^2 \tag{8}$$

where ρ is the fluid density and g is the gravitational acceleration. Given the quadratic relationship between E_i and R_i , similar frequency distribution trends are observed between these two parameters for different constituent sets. The range of E_i for 2 constituents is narrow with high accumulation in minimum and maximum values (as in Fig. 4a for R). With increasing k , distributions become wider. Indicatively,

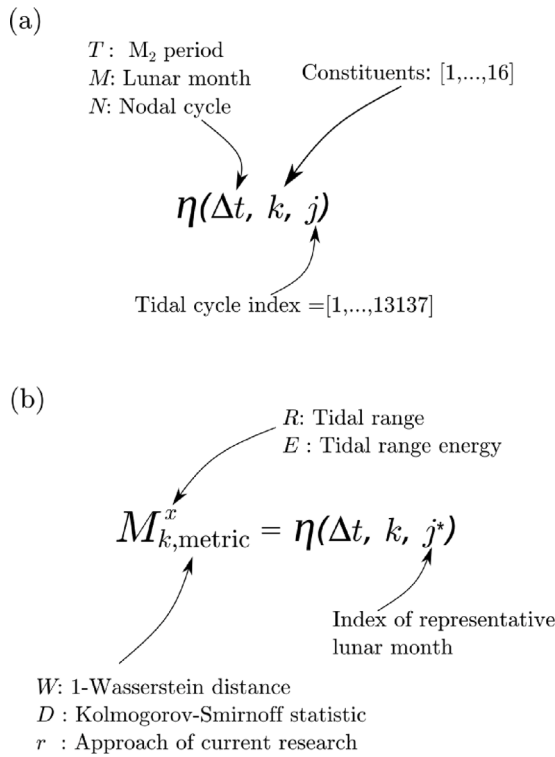


Fig. 3. Sketch of notation employed in this study. (a) Notation of η elevation-time interval. The tidal cycle index indicates the start of the interval at the beginning of M_2 cycle j . (b) Representative month corresponding to an η elevation-time interval. x denotes whether the tidal range characteristics (R, H_m) or energy (E, \overline{PE}) are considered as the quantity of interest. The subscript ‘metric’ indicates the strategy to identify the representative month.

the maximum E_i for 12 constituents is approximately 30% and 40% greater for Avonmouth and Llandudno respectively compared to the case of 2 constituents. Furthermore, we observe significant differences in their mean value over the nodal cycle. That is, the mean of E_i for 12 constituents is higher by 11% at Avonmouth and 5% at Llandudno.

Consistently to the notation for the arrays of tidal range values, we denote as $\tilde{E}(M, k, j)$ and $\tilde{E}(N, k, 1)$, arrays containing the theoretical available energy E_i within the j th lunar month M and the nodal cycle N respectively.

3.4.2.2. Average potential energy \overline{PE} . As with R_i, E_i relies on discrete points rather than the entire tidal signal. We thus also consider the average potential energy contained over time in tidal waves. Considering the wave shown in Fig. 5, integrating over time, the potential energy of a wave averaged over an interval $\Delta t = t_{i+1} - t_i$ is [51]:

$$\overline{PE}(t_i, \Delta t) = \frac{1}{\Delta t} \int_{t_i}^{t_i+\Delta t} \frac{\rho g (h + \eta)^2}{2} dt \quad (9)$$

Noting that the depth h contributes to the hydrostatic energy of the water column and our focus is solely on the potential energy of the surface wave, h can be excluded by considering as datum the mean water level (MWL). For completeness, in the case the sea surface η is represented by k constituents, the average potential energy is given by

$$\Sigma \overline{PE} = \frac{\rho g}{16} \sum_{i=1}^k H_i^2 \quad (10)$$

in which $H_i = 2\alpha_i$ is the wave height of each constituent. Similarly to the amplitude of constituents we define a participation percentage $\overline{PE}_i / \Sigma \overline{PE}$ to account for the influence of constituents on the total average potential energy as in Table 2.

3.4.3. Extractable tidal range energy E_{0D}

Having established the basic tidal wave quantities, we investigate the link between the technically extractable energy through the operation of tidal range structures and the available resource. Our approach hypothesises the deployment of idealised tidal lagoons at sites that feature promising levels of potential energy to be exploited (Fig. 2). Neill et al. [2] assumes a minimum acceptable annual yield of 50 kWh/m² based on an average $\bar{R} = 5$ m. We adopt a more conservative approach with a minimum $\bar{R} = 7$ m, based on previous proposals such as the Swansea Bay tidal lagoon that were narrowly dismissed on feasibility grounds despite their greater tidal range. This threshold returns a minimum acceptable annual yield of 94 kWh/m². A constant impounded surface area $A_s = 1$ km² is assumed. The deployment of schemes of this scale is considered small and thus we assume that regional tidal hydrodynamics are not affected. Furthermore, we assume that this hypothetical scheme will not be influenced by intertidal area effects [15,16], meaning that the water volume in the impoundment linearly varies with the water depth [15].

In quantifying the portion of the theoretical potential energy that can be extracted we proceed to simulate the operation of tidal range structures, using the 0-D modelling of Angeloudis et al. [25]. The 0-D model is based on an explicit backward finite difference approach which adheres to the principles of mass conservation. This method essentially uses the head difference to determine the volume exchange between the seaward and impounded water levels at a given timestep. This type of modelling is commonly used in tidal range energy and optimisation studies [8,20,21,25,30,49] due to its high computational efficiency.

As we consider idealised schemes, certain decisions must be made on the hydraulic structure configuration to ensure consistency across sites [28]. This requires the determination of a sensible number of turbines and sluice gates [52], subject to the available potential energy [15]. We follow the methodology used in Neill et al. [40] to determine a desired configuration based on the average potential energy. The predicted capacity is defined as

$$C = \eta_e \frac{\rho g A_s \bar{R}^2}{T_{M_2} C_F} \quad (11)$$

where η_e is the expected generation efficiency, \bar{R} is the mean annual tidal range and C_F is a capacity factor. We set $\eta_e = 0.40$ following the estimate of 37% by Burrows et al. [9] for two-way operation. In turn, acknowledging economic feasibility constraints we choose $C_F = 0.20$, providing a break even target for the installed capacity. The number of turbines and sluice gates is empirically defined as $N_t = C/P_{\max}$ and $N_s = N_t/2$ respectively, with P_{\max} the turbine rated power, in compliance with the available resource by setting the turbine rated head to $0.8\bar{R}$. This modulation of rated head is introduced to ensure a fair comparison across sites tailoring the turbine parametrisation to the respective site. More details on the turbine Hill chart parametrisation can be found in Aggidis and Feather [21] and Angeloudis et al. [25], which are omitted here for brevity.

A two-way operation regime (see green line of Fig. 5) is considered, as the corresponding generation window covers a greater proportion of the tidal cycle compared to one-way generation and preserves the tidal range conditions within the impoundment as much as possible [2]. Moreover, it represents the default operation for recent proposals and studies [17,23,25,28,40]. Finally, as the plant performance closely relates to the power plant mode scheduling [40], we explore two operation control strategies; one fixed/conservative and one flexible/adaptive. For the fixed control, we set a holding period of 3 h both under ebb and flood conditions. In the latter, these parameters are optimised in time for the tidal range plants at each location. The optimisation of operation follows the approach of [8,28], adopting an energy maximisation objective function spanning two-cycles of oper-

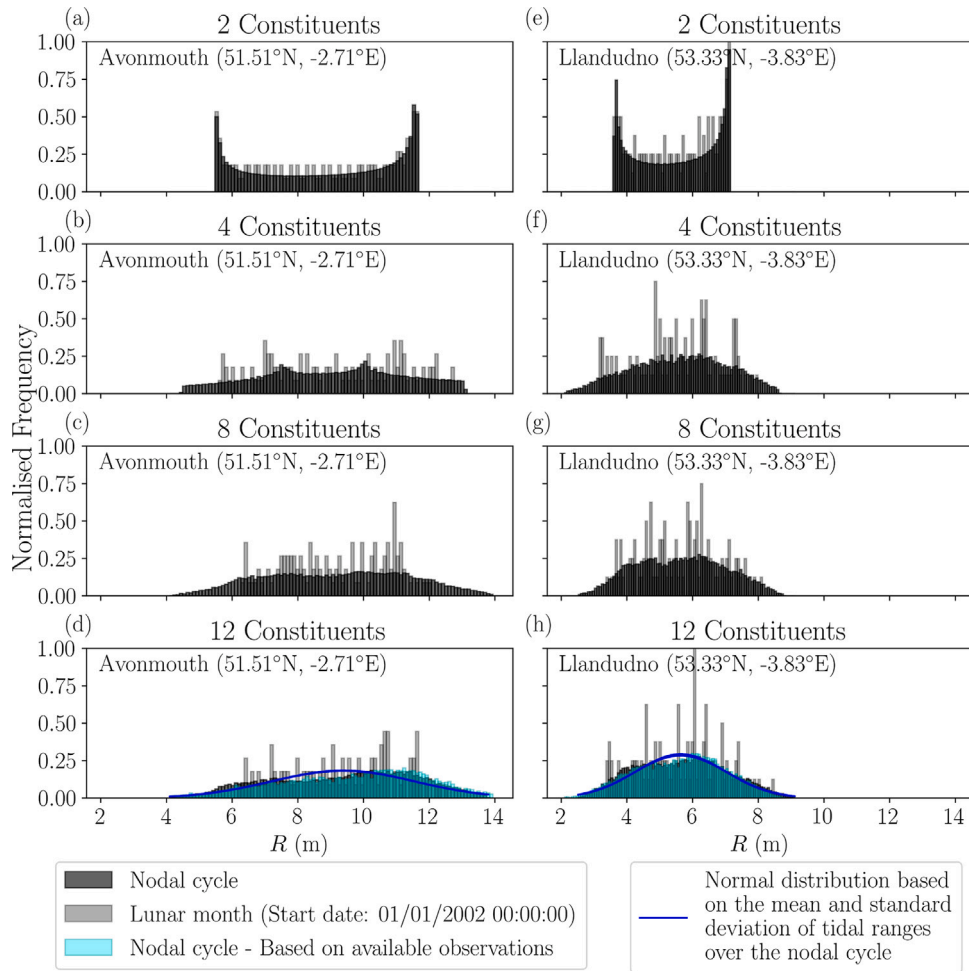


Fig. 4. Tidal range histograms for elevation-time signals at Avonmouth and Llandudno under (a, e) 2, (b, f) 4, (c, g) 8, and (d, h) 12 constituents (selected in order of a descending magnitude) for a lunar month (grey) and a nodal cycle (black). Cyan bars illustrate the distribution of R based on available observations. The normalised frequency is the number of entries in each bin divided by the total number of counts and the bin width. The bin width is equal to 0.1 m.

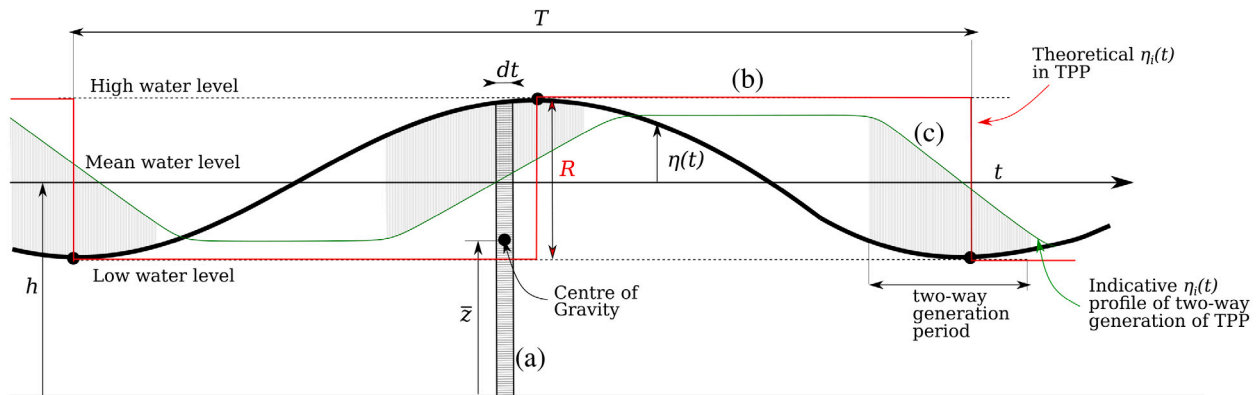


Fig. 5. Definition sketch for (a) the total wave potential energy, the impounded area elevation profile for (b) the maximum theoretically extractable energy operation (red) and (c) for a typical two-way operation (green) associated over a period T .

ation. The 0-D model was forced using signals for $k \in \{2,4,8,12\}$. Simulations included 10 tidal cycles of spin-up and then spanned the same full nodal cycle starting on 01/01/2002 00:00:00.

As with E_i and \overline{PE} , we define equivalent metrics associated with the technically extractable energy. The 0-D energy output prediction

over a period $\Delta t = t_{i+1} - t_i$ is given by:

$$E_{0D,i}(t, \Delta t) = \int_{t_i}^{t_i+\Delta t} P(t) dt \tag{12}$$

where $P(t)$ is the power output. Each tidal cycle consists of two transitions; one from HW to LW and vice versa. Thus, in correlating $E_{0D,i}$ to E_i , we consider the associated energy over half tidal cycles; that is, we set $\Delta t = \frac{T}{2}$. $E_{0D,i}$ is in turn aggregated in \mathcal{G} consistently

with the tidal range and potential energy quantities. Next, we define the average 0-D energy output over an arbitrary period Δt as

$$\overline{E_{0D}}(t_i, \Delta t) = \frac{1}{\Delta t} \int_{t_i}^{t_i+\Delta t} P(t)dt, \tag{13}$$

rendering it comparable to \overline{PE} (Eq. (9)). In examining the generated energy relative to the available resource over each transition i , we define the efficiency factor

$$\eta_{g,i} = \frac{E_{0D,i}}{E_i}, \tag{14}$$

and by extension, we denote as $\bar{\eta}_g$ the average efficiency.

3.5. Metrics

We apply three nonparametric metric-based approaches to assess the representative quantity distributions, spanning the Kolmogorov–Smirnov test, the Wasserstein distance, and a custom approach. The former are widely applied distribution statistics, while the latter is based on the quantities of Section 3.4.

3.5.1. Kolmogorov–Smirnov test

The two-sample Kolmogorov–Smirnov (K-S) test is one of the most commonly used goodness-of-fit methods for quantifying the resemblance of two distributions [53] by comparing their cumulative distribution functions (CDFs). The K-S test computes the statistic $D_{m,n}$:

$$D_{m,n} = \max |F_{\mathcal{X},m}(x) - F_{\mathcal{X}^*,n}(x)|. \tag{15}$$

It measures the maximum discrepancy corresponding to empirical CDFs ($F_{\mathcal{X}}, F_{\mathcal{X}^*}$) of the samples \mathcal{X} and \mathcal{X}^* (of size m and n respectively). This approach is sensitive to detect differences in both the location and the shape of the empirical cumulative distribution functions of the two samples [53].

3.5.2. Wasserstein distance

The p -Wasserstein distance W_p is another measure of similarity between distributions. [54]. W_p can be defined in several ways based on the order p ; the interested reader is referred to Ramdas et al. [55] for a detailed description. In this study we focus on the 1-Wasserstein distance. Consistent to the notations of $D_{m,n}$ the 1-Wasserstein distance of two random samples is

$$W_1 = \int_{\mathbb{R}} |F_{\mathcal{X},m}(x) - F_{\mathcal{X}^*,n}(x)| dx, \tag{16}$$

which is equal to the area between the two CDFs.

3.5.3. Custom metrics on magnitude and variability

Finally, we introduce two metrics for the *magnitude and variability* based on the quantities of Section 3.4. For magnitude, we use the median P_{50} ; that is, the 50th percentile value, preferred as a resistant measure that is not strongly influenced by a few extreme values. For variability, we use the interquartile range (IQR), a non-parametric resistant measure of spread of data [56]. This measures the range of 50% of data, discounting the lower and upper 25th and 75th percentiles respectively. The first metric, \mathcal{M}_1 , makes use of the discrete quantities so that $\mathcal{X} \in \{\bar{R}, \bar{E}, \bar{G}\}$ as

$$\mathcal{M}_1 = \alpha \times |P_{50}(\mathcal{X}) - P_{50}(\mathcal{X}^*)| + \beta \times |IQR(\mathcal{X}) - IQR(\mathcal{X}^*)| \tag{17}$$

where α and β are weight factors (in this case $\alpha = \beta = 0.5$). \mathcal{M}_1 effectively considers the 1-D array \mathcal{X} over a particular period (e.g. a lunar month M) relative to the equivalent \mathcal{X}^* of a different duration (e.g. a nodal cycle N).

We then consider a second metric, \mathcal{M}_2 based on $\mathcal{Y} \in \{H_{m0}, \overline{PE}, \overline{E_{0D}}\}$ as

$$\mathcal{M}_2 = |\mathcal{Y} - \mathcal{Y}^*| \tag{18}$$

where $\mathcal{Y}, \mathcal{Y}^*$ represent the same quantities over a different timeframe.

Focusing on tidal range R as an example, $\mathcal{X} = \bar{R}(M, k, j)$ and $\mathcal{X}^* = \bar{R}(N, k, 1)$ in Eq. (17). In turn, in Eq. (18), $\mathcal{Y} = H_{m0}(M, k, j)$ and $\mathcal{Y}^* = H_{m0}(N, k, 1)$. By extension, in the case of tidal range energy, the \mathcal{X} and \mathcal{Y} arguments are replaced by the equivalent \bar{E} sets and \overline{PE} values.

3.6. Rating lunar month periods

Having established these metrics, we can identify the most representative lunar month M relative to a nodal cycle N . Using an iterative approach that considers each lunar cycle, values of $D_{m,n}$, W_1 , \mathcal{M}_1 and \mathcal{M}_2 are calculated for varying k and target representative quantities (tidal range, available energy, extractable energy).

As the range of values for each metric varies we define a rating system to facilitate comparison. This entails a normalisation process whereby the rating score RS over the j th lunar month is given as

$$RS_{\text{metric},j} = 1 - \frac{\min(\text{metric}) - \text{metric}_j}{\max(\Delta\text{metric})} \tag{19}$$

where $\text{metric} \in \{\mathcal{M}_1, \mathcal{M}_2, D_{m,n}, W_1\}$. In doing so, we obtain a rating scale from 0 (poor) to 1 (excellent). For the custom approach we denote $RS_r = (RS_{\mathcal{M}_1} + RS_{\mathcal{M}_2})/2$. For all metrics, the corresponding timeframe of the maximum RS value is selected as the optimal representative lunar month. We denote the elevation time-series corresponding to this period as $M_{k,r}^R$ and $M_{k,r}^E$ regarding tidal range and energy quantities respectively as per Fig. 3b. Accordingly, we denote $M_{k,D}^R, M_{k,W}^R$ and $M_{k,D}^E, M_{k,W}^E$, for the maximum ratings RS_D, RS_W of $D_{m,n}$ and W_1 respectively.

4. Results

4.1. Validation of harmonic analysis reconstruction

Reconstruction of tidal signals is performed across sites where BODC data are available. The contribution of constituents beyond the leading (i.e. most dominant) $k = 12$ in the total amplitude are marginally influential as presented in Table 2. Thus, given further data gaps in tide gauge records that add to the uncertainty, we consider $k = 12$ as the baseline for our analysis. NRMSE and R^2 for the locations of highest range are shown in Fig. 6 with respect to k . The largest NRMSE and the smallest R^2 were predicted at Avonmouth where $\Sigma\alpha$ is greatest (8.98 m). This is also expected due to the pronounced non-linear shallow water hydrodynamics present at estuarine regions. As expected, the greater the k number, the lower the NRMSE, and the larger the R^2 , corresponding to greater correlation between modelled and recorded tidal surface elevations. We can see that for $k \in \{1, ..7\}$ the curvature of the corresponding plots is steep suggesting a significant influence. Indicatively, the absolute percentage differences of metrics for $k = 12$ relative to $k = 2$ are on average 5.7% and 58.7% for R^2 and NRMSE respectively. The equivalent percentage differences for $k = 16$ are 5.8% and 61.4% respectively, and thus of marginal improvement.

4.2. Effect of tidal signal duration on target representative quantities

As in Fig. 4, there are noticeable differences in the lunar-monthly and nodal distribution of R_j . This motivates investigating sensitivity in extending the tidal signal timeframe, and evaluating resemblance against the nodal distribution. We apply Eq. (15) and consider tidal signals of a variable timeframe but with a fixed start date (01/01/2002 00:00) for $k = 12$. In Fig. 7a the cumulative distribution functions (CDF) of 1-, 2 and 6-month samples, as well as the point where the K-S metric $D_{m,n}$ value is recorded. We notice that, 1- or 2-month samples deviate from the nodal cycle distributions by a $D_{m,n}$ of 0.12 and 0.07 respectively. Increasing the sample duration to 6 months results in a $D_{m,n}$ of 0.04. A more detailed quantification of the differences in distributions is depicted in Fig. 7b which presents how $D_{m,n}$ varies

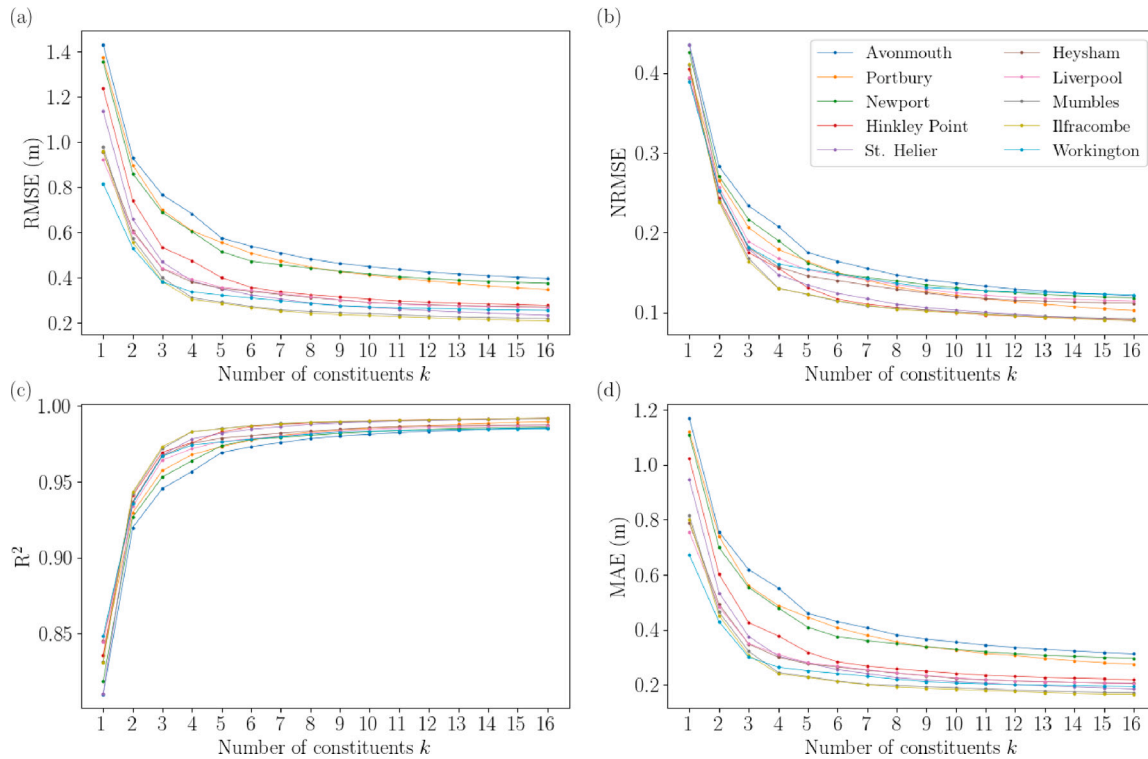


Fig. 6. Comparative metrics of predicted and observed water elevations in the top ten locations with the highest aggregated amplitude $\Sigma\alpha$. (a) Root mean square error (RMSE). (b) Normalised root mean square error (NRMSE). (c) Coefficient of determination R^2 . (d) Mean average error (MAE).

under tide signals of varying lunar month timeframes. We notice in general, a downward trend as the signal duration increases.

In Fig. 7b for the timeframe of a single lunar month, $D_{m,n}$ varies from 0.04 to 0.26. The best possible value (0.04) of one lunar month samples is equal to the $D_{m,n}$ of the randomly selected six-month sample of Fig. 7a. Effectively, $M_{12,D}^R$ provides a good resemblance to the nodal CDF as validated in Fig. 7c. Equivalent conclusions are obtained when we investigate the behaviour of W_1 , as presented in Fig. 7c,d. The CDF of $M_{12,r}^R$ is also plotted in Fig. 7c with a satisfactory correspondence to the nodal distribution. In Fig. 7b,d we see the values of $D_{m,n}$ and W_1 lying at the lower margin of the metric value for $M_{12,r}^R$, $M_{12,D}^R$ and $M_{12,W}^R$.

4.3. Representative month identification and observations

Focusing on tidal range and energy statistics, we observe how these vary spatially, subject to the consideration of different constituent sets k . Fig. 8 presents how the \overline{PE} and $IQR(\vec{\mathcal{E}})$ of the representative months $M_{k,r}^E$ for $k \in \{2, 4, 8, 16\}$, deviates from the baseline signal, reconstructed for $k = 12$ spanning a nodal cycle N . The range of $\overline{PE}(M, 12, j)$ varies by 13.8%–30% (with an average value of 21.2%) across gauges (Fig. 8c). Interestingly, we notice that the tidal range energy variability using IQR exhibits a much higher variation of over 45% (Fig. 8a). Despite the deviation range across gauges, we observe a convergence to baseline predictions for both \overline{PE} and $IQR(\vec{\mathcal{E}})$, once $k \geq 8$.

The MAE across gauges for $k = 8$ with regards to \overline{PE} and $IQR(\vec{\mathcal{E}})$ is 0.7% and 4.7% respectively. The latter would be considered acceptable given additional non-tidal uncertainties. For $k = 16$, we obtain equivalent MAEs as for $k = 8$, affirming the convergence to representative months beyond this point for the UK tidal system. While the above results refer to the potential energy content, equivalent results are acquired for tidal range quantities. In Fig. 8a,c the case of $M_{12,r}^R$ is included to highlight that relative errors do not vary from the baseline. Accordingly, this extends to observations for $H_{m_0}(M, 12, j)$

and $IQR(\vec{\mathcal{R}}(M, 12, j))$ (results are not plotted for brevity) for both their margins of deviation and the convergence when applying $M_{k,r}^R$ and $M_{k,r}^E$. In fact, for 12 out of the 46 locations $M_{k,r}^R$ and $M_{k,r}^E$ correspond to the same timeframe.

We then examine the application of metrics $D_{m,n}$ and W_1 on capturing the representative nodal quantities of interest. We observe minor discrepancy compared to $M_{k,r}^R$ and $M_{k,r}^E$ for different k values. Indicatively, the \overline{PE} and $IQR(\vec{\mathcal{E}})$ of $M_{12,D}^E$ and $M_{12,W}^E$ differs from the equivalent quantities of $M_{12,r}^E$ by 0.8% and 2% on average. Considering the metric $D_{m,n}$, tidal range and energy representative months for $k \geq 8$ coincide across all locations. In the case of W_1 , we have agreement in 25 gauges and the rest display a very good rating when applied simultaneously.

4.4. Analysis timeframe impact on expected power generation

In correlating the available resource with the tidal signal variability on extractable energy, lunar-monthly $E_{0,D,i}$ were calculated for each idealised power plant for both fixed and flexible two-way power generation operation. Given the previously stated annual energy threshold of 94 kWh/m², only the top 11 gauges of Fig. 2 are included in this analysis.

First, we quantify the available and technically extractable energy and assess their correlation using the Spearman coefficient (r_s ; [57]). The sites considered exhibit a r_s from 0.92 to 0.97 when comparing $\vec{\mathcal{E}}(N, 12, 1)$ and $\vec{Q}(N, 12, 1)$. Fig. 9a and b illustrate an example of this strong correlation in Avonmouth. Relative regression lines are fitted to explore trends between datasets (Fig. 9b). For a fixed operation, $R^2 = 0.94$ between actual data and the estimated second order polynomial regression response. In the case of flexible operation, $R^2 = 0.91$ using a linear relationship.

Fig. 10a illustrates how $IQR(\vec{\mathcal{E}}(M, 12))$ affects the generation efficiency $\bar{\eta}_g$ at Avonmouth. Under a fixed operation, $\bar{\eta}_g$ reduces with the increase of $IQR(\vec{\mathcal{E}}(M, 12))$; When power generation optimisation is considered, this effect is mitigated. By extension, Fig. 10b explores

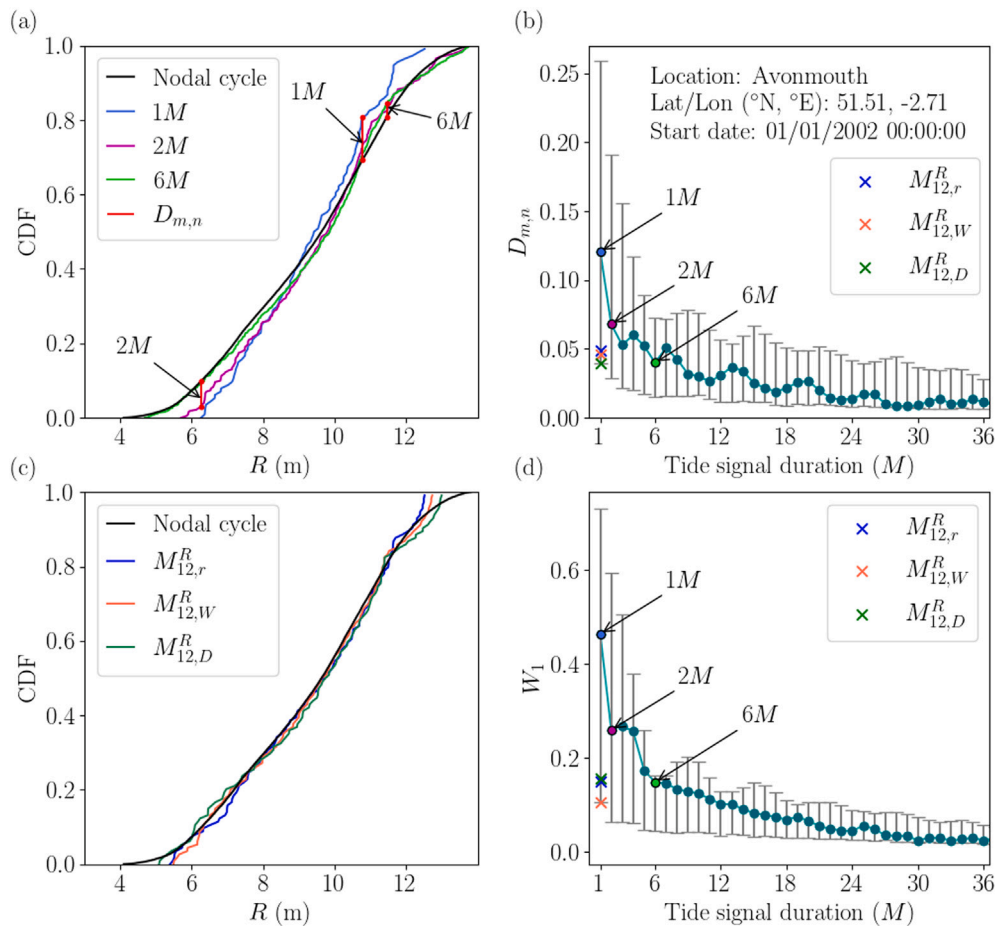


Fig. 7. Comparison of tidal range distributions at Avonmouth for signals spanning varying lunar months (M) relative to a nodal cycle case for 12 constituents. (a) Cumulative distribution functions (CDFs) of random lunar month samples of varying duration (1, 2 and 6M). (b) $D_{m,n}$ vs signal duration. (c) CDFs of representative months for different metrics. (d) W_1 metric sensitivity to signal duration. In (b) and (d) error bars indicate the uncertainty range when start dates of tidal signals are variable. The markers indicate the values for signals starting on 01/01/2002 00:00:00.

correlations between $\bar{\eta}_g$ and $IQR(\vec{\mathcal{E}}(M, 12))$ across sites. The average r_s under fixed operation is equal to -0.85 , indicating a very strong negative correlation. In contrast, under flexible operation the average $r_s = -0.49$; that is, a moderate negative relationship, indicating that the optimisation tangibly corrects this trend.

4.5. Spatial sensitivity of representative month target quantities

Having established the representative months, we investigate the spatial variation for implications to engineering assessments (e.g., tidal range plants). Fig. 11 illustrates the spatial behaviour of representative months in Avonmouth. We observe that when these are applied simultaneously across tide gauge sites, corresponding errors for \overline{PE} , $\overline{E_{0D}}$ and associated IQR are confined. Indicatively, the MAE in \overline{PE} is 0.7%, 1.5% and 0.9% for $M_{k,r}^E$, $M_{k,D}^E$ and $M_{k,W}^E$ respectively. While, the corresponding errors in $IQR(\vec{\mathcal{E}})$ are 5.5%, 5.0% and 6.5% respectively. Additionally, Fig. 11 provides insights into how the representative months perform under a flexible generation regime, over those periods. Indicatively, the MAE in $\overline{E_{0D}}$ is 0.9%, 1.6% and 1.2% for $M_{k,r}^E$, $M_{k,D}^E$ and $M_{k,W}^E$ respectively. Considering $IQR(\vec{\mathcal{G}})$, the corresponding errors are 7.9%, 7.6% and 5.7%.

5. Discussion

5.1. On the reconstructed signals

The statistical analysis indicates an overall good agreement between observed and reconstructed water levels once $k \geq 8$ (see Fig. 6) based

on related comparative metrics values found in existing literature [18]. However, apart from the tidal components that make up the observed system, even if the UK coastal ocean is classed as macrotidal [58], there are non-tidal contributions that are neglected in the reconstruction process. These include contributions from storm surges [59,60] as well as non-linear wave transformation in shallow regions. These have been quantified as 3%–4% on an annual basis; however, short-term effects over a lunar month could skew conclusions. This invariably leads to deviations between observed and reconstructed data. This is indicated in Fig. 6, where we observe that the comparative metrics exhibit no further significant convergence with the addition of constituents beyond around 12. As discussed previously, most uncertainty arises in areas of the greatest resource. This becomes more apparent by observing the RMSE and MAE in Fig. 6a,d. We notice that Avonmouth, Portbury and Newport, being closest to the tidal limit of the Severn estuary, exhibit the largest deviations, with these being significantly greater compared to other sites.

The accuracy of predicted water levels is critical in any feasibility assessment of tidal range plant as well as related environmental impact. Apart from historical data, tidal elevation time-series may also be generated from 2-D hydrodynamic models. Regardless of their source, other factors may be influential in producing erroneous water levels. These include a variety of mechanisms as reported in Hanousek and Ahmadian [61], such as substantial wave effects, miscalculations on associated water level, faulty readings, incorrect modelling assumptions and improperly identified time zone. This motivates further research in comprehensive uncertainty quantification with models that seek to account for local hydrodynamics.

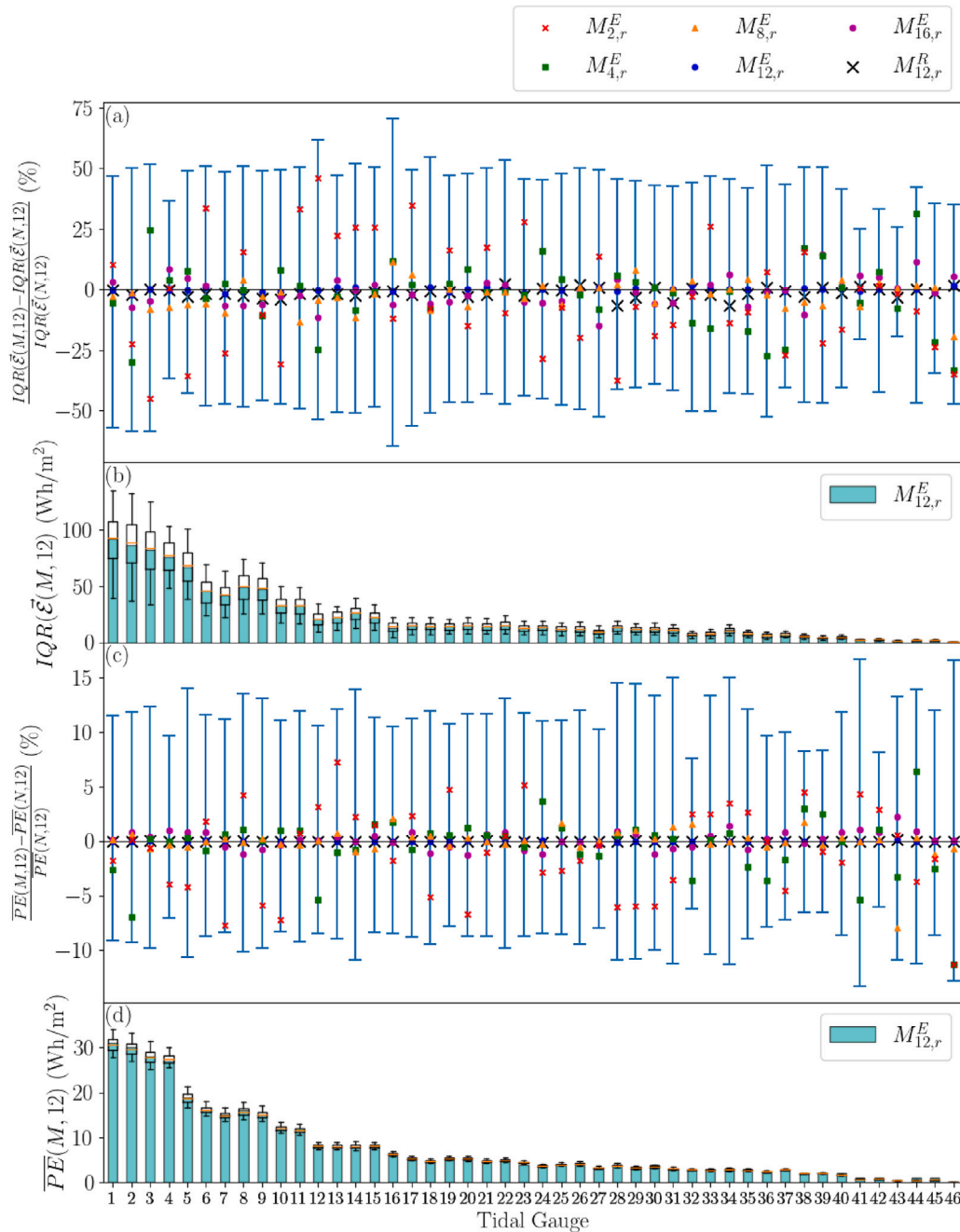


Fig. 8. Relative deviation of (a) $IQR(\bar{\epsilon}(M, 12))$ and (c) $\overline{PE}(M, 12)$ of representative months to the baseline $IQR(\bar{\epsilon}(N, 12))$ and $\overline{PE}(N, 12)$ respectively, in tide gauge stations for a varying constituent set k . Values are plotted based on the representative month at each location. Blue bars indicate the range of related variables across lunar cycles. Bar charts illustrate the expected (b) $IQR(\bar{\epsilon}(M, 12))$ and (d) $\overline{PE}(M, 12)$ of $M_{12,r}^E$ at all locations. Box plots represent the statistical range of $IQR(\bar{\epsilon}(M, k, j))$ and $\overline{PE}(M, k, j)$ for $k = 12$ constituents.

5.2. On the influence of constituent set k on representative months

In Table 2 we notice that the contribution of constituents for $k \geq 4$ in the total average potential energy ΣPE is very small. However, focusing on the definition of ΣPE , it does not account for phase differences between the different constituents (see Eq. (10)). It is defined over recurring signals over long-term periods i.e, a nodal cycle. It is expected that the contribution of other constituents becomes more noticeable over constrained periods when phase differences becomes more significant as indicated by Fig. 7. Indeed, findings suggest that the constituents set k used for defining representative lunar months has substantial significance to the level of errors in quantities of interest against the baseline scenario of $k = 12$. The results illustrate (Fig. 8)

that in most cases using 2–4 constituents, the associated $M_{k,r}^E$ can have a large range of relative errors that can lead to a major deviation from the actual target representative quantities. On the other hand, while maximising the number of constituents considered is encouraged, errors are contained above $k = 8$. Consistent findings are obtained when assessing the application of $M_{k,D}^E$ and $M_{k,W}^E$.

5.3. On the representative month identification strategy

Tidal range R , associated energy E and predicted energy output E_{0D} are seen to possess a degree of consistency for representative months. An example of this consistency is presented in Table 3 which shows the representative rating of energy-based representative months

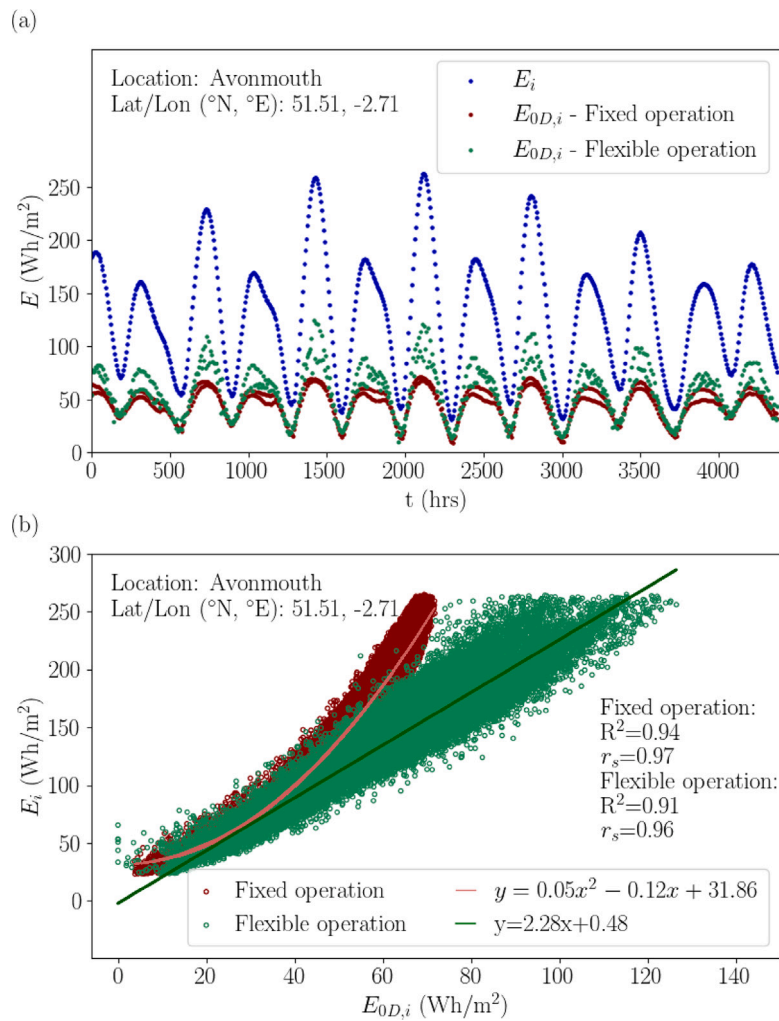


Fig. 9. Comparison of E and E_{0D} under fixed and flexible operation. (a) E_i and $E_{0D,i}$ for each transition in Avonmouth. (b) E_i vs $E_{0D,i}$ in Avonmouth. R^2 is the coefficient of determination between the data and the corresponding regression line. r_s the Spearman correlation between $\tilde{E}(N, 12, 1)$ and $\tilde{Q}(N, 12, 1)$.

in Avonmouth when assessed simultaneously by other metrics. These metrics are in turn extended to the extractable energy values for a flexible operation as this option captures most of the available resource (see Fig. 9a,b and Section 5.4.2). All representative months perform well, given their rating is ≥ 0.80 in all cases. Focusing on the rating values for Avonmouth and considering the mean representative month ratings, they show the following relationship: $M_{12,W}^E > M_{12,r}^E > M_{12,D}^E$ (with values 0.98, 0.97 and 0.94 respectively). Under a flexible operation, this relationship is preserved with corresponding average ratings of 0.90, 0.88 and 0.83. It appears that, locally, representative months $M_{12,r}^E$, $M_{12,W}^E$, $M_{12,D}^E$ show encouraging performance compared to ratings in studies from literature (Table 3).

Furthermore, findings show that representative months for tidal range ($M_{k,metric}^R$) and energy ($M_{k,metric}^E$) provide equivalent RS_{metric} for the same timeframe. For RS_r this is a result of the \mathcal{M}_2 metric that includes the integration of elevation η quantities over the interval for both tidal range and energy quantities. Similarly, $D_{m,n}$ and W_1 metrics that concentrate on tidal range or energy cumulative distributions, appear robust whether we use R or E given the baseline quadratic relationship between the two quantities.

In practice, when comparing tidal range schemes at different locations (e.g., a barrage in the Severn Estuary and a lagoon along the North Wales coast) we are interested in assessing whether the same lunar cycle could be used for a comparative assessment. This could be particularly important when we might have surface elevation data for

one location and we want to assess the performance of a scheme in a site where access to data is restricted. As such, it is instructive to review the behaviour of representative months in Avonmouth when applied to the other locations. We observe that the deviation margin in the quantities we examine is consistent while $k \geq 8$ (see Fig. 11 for $k = 12$). In this way a level of uncertainty (e.g $\pm 11\%$ for \overline{PE}) associated with the available resource is contained when considering the operation of tidal range power plants. Extending this to the extractable energy, we see that errors to the \overline{PE} and $\overline{E_{0D}}$ baseline can similarly be constrained. On the other hand, related IQR show a greater degree of variation. This is probably due to the influence of local hydrodynamics or other modes of errors as previously mentioned; further research accounting for hydrodynamics is required. It should be noted that although Portbury (tidal gauge 2) is in proximity to Avonmouth (tidal gauge 1) we observe a degree of divergence. A possible explanation for this is the low availability of recordings at Portbury (Fig. 2) that could influence the accuracy of the reconstructed signal, highlighting how lack of computational data or accuracy is an issue towards establishing a reliable tidal signal in engineering applications.

The qualitative performance of representative months based on Avonmouth when rated across the rest of the tide gauge network is statistically explored in Table 3. First, for each metric we consider the average value of ratings denoted as \overline{RS}_{metric} . Taking the mean of \overline{RS}_{metric} for each representative month, we notice that they are of equivalent magnitude; that is, 0.86–0.87. Under a flexible operation,

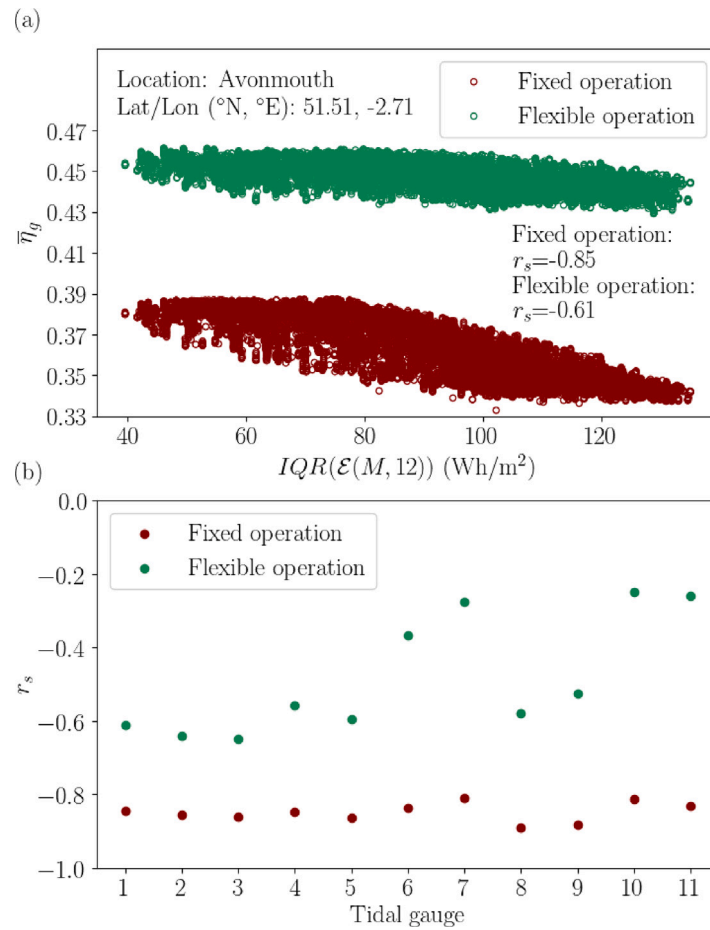


Fig. 10. Relationship between $\bar{\eta}_g$ and $IQR(\bar{\mathcal{E}}(M, 12))$ under fixed and flexible operation. (a) $\bar{\eta}_g$ vs $IQR(\bar{\mathcal{E}}(M, 12, j))$ in Avonmouth. (b) r_s between the groups containing all $\bar{\eta}_g$ and $IQR(\bar{\mathcal{E}}(M, 12, j))$ over the nodal cycle, for the 11 most energetic locations.

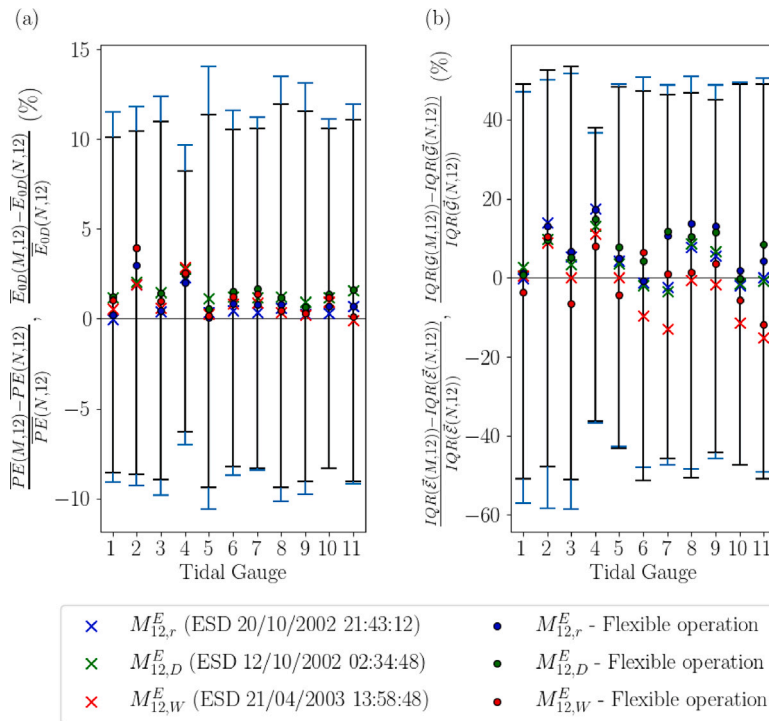


Fig. 11. Comparison of (a) $\overline{PE}(M, 12)$ vs $\overline{PE}(N, 12)$, and (b) $IQR(\bar{\mathcal{E}}(M, 12))$ vs $IQR(\bar{\mathcal{E}}(N, 12))$, for representative energy months for Avonmouth. Blue bars indicate the range of $\overline{PE}(M, 12)$ and $IQR(\bar{\mathcal{E}}(M, 12))$; while, black ones display the range of $\overline{PE}(N, 12)$ and $IQR(\bar{\mathcal{E}}(N, 12))$.

Table 3

Rating score RS of strategies r , $D_{m,n}$ and W_1 for representative months $M_{12,r}^E$, $M_{12,D}^E$, $M_{12,W}^E$ in Avonmouth. Variables with overline correspond to the average rating over the top 11 most energetic locations identified for tidal range energy extraction.

		$M_{12,r}^E$	$M_{12,D}^E$	$M_{12,W}^E$
Tidal range energy - (\bar{E} , \overline{PE}):				
Avonm.	RS_r	1.00	0.91	0.97
	RS_D	0.96	1.00	0.97
	RS_W	0.94	0.91	1.00
11 Loc.	$\overline{RS_r}$	0.89	0.86	0.88
	$\overline{RS_D}$	0.88	0.90	0.87
	$\overline{RS_W}$	0.81	0.83	0.87
Flexible operation - (\bar{G} , $E_{0,D}$):				
Avonm.	RS_r	0.94	0.85	0.89
	RS_D	0.89	0.81	0.91
	RS_W	0.80	0.84	0.90
11 Loc.	$\overline{RS_r}$	0.85	0.81	0.85
	$\overline{RS_D}$	0.81	0.82	0.88
	$\overline{RS_W}$	0.80	0.80	0.86

average ratings are 0.87, 0.82 and 0.81 for $M_{12,W}^E$, $M_{12,r}^E$ and $M_{12,D}^E$ respectively. It appears that the use of the combination of our custom metrics M_1 , M_2 as well as the metrics W_1 , $D_{m,n}$, in identifying representative periods, maintain overall good average ratings spatially. Therefore, they could be used to obtain comparative conclusions across schemes at different locations.

5.4. On implications for tidal range energy assessments

The results revealed a large range of deviation of lunar-monthly to nodal quantities of interest. Given this margin of deviation, the selection of a particular constrained interval for the analysis can result in a major under- or overestimation of the tidal range magnitude or the available energy. This indicates the importance of selecting a representative period when independent studies are conducted.

5.4.1. Timeframe selection impact on resource assessment

We previously summarised the timeframes used in previous studies (Table 1) with a view to assess how well the target representative quantities of interest \overline{PE} and $IQR(\bar{E})$ are captured. This is not an attempt to question the accuracy of these studies but an opportunity to demonstrate the implications of the present analysis. In calculating the rating score for each study, our reconstructed signal was sampled over the analysis timeframe reported. Taking into account the spatial correlation of representative months, we consider the metrics of the resulting tidal signals (represented by $k = 12$) at Avonmouth as a comparative measure. We observe a variety of differences to nodal target quantities. For instance, the simulation period of Angeloudis and Falconer [23] returns a relatively small deviation of 3.1% for \overline{PE} , but $IQR(\bar{E})$ deviates significantly with 42.3% error and a moderate performance based on the rating of the metrics. Out of the studies reported, only a minority [18,29] return encouraging lunar-month ratings.

Extending the simulation period in [29] from 0.5M to 1M results in an improvement of metric values. Indicatively, errors with respect to \overline{PE} improved from -3.2 to -0.8%. However, errors in $IQR(\bar{E})$ persist (from -8.8 to 8.6). This highlights again that the duration of the tidal signals has a large influence on capturing related nodal conditions. It is expected that deviations from nodal cycle target quantities to be reduced in longer timeframes e.g. when considering a year-long duration (12.4M). For instance, in year-long studies [20–22] where the start date of annual simulations is not provided we predict that $\overline{PE}(12.4M, 12)$ lies between -1.3 and 1.5% to the target $\overline{PE}(N, 12)$. For $IQR(\bar{E})$ the corresponding range is from -8 to 8%. This indicates that year-long tidal segments are adequate in capturing representative

quantities (as in Fig. 7b,d). However, this may result in a greater computational cost for associated simulations, as a robustly calibrated model would need to be established for extended periods.

5.4.2. Timeframe selection impact on operational performance

The technical extractable energy from tidal range plants is closely linked to both the theoretically available resource and the associated variability as in Fig. 9a and the high r_s values of Fig. 9b. We observe that operation optimisation primarily benefits energy conversion over high resource tidal cycles (e.g., spring tides). This is confirmed by the regression lines, where R^2 values indicate a very good fit. There is consistently superior power generation under flexible operation and only a small region of overlap with the fixed operation one. Indicatively, this overlapping occurs in the region where E_i lies between 50–70 Wh/m² or equivalently for R between 6–7 m. The significance of the influence of spring-neap variability on generated energy is highlighted beyond this region.

A bias in a tidal range energy analysis could stem from tide’s variability (represented here through $IQR(\bar{E})$), given that studies to-date prioritise matching the mean energy content. Specifically, when $IQR(\bar{E})$ is higher, tidal range and associated energy are greater. A higher $IQR(\bar{E})$ would also lead to a further under-performance of fixed operation, as shown by the deviation of fixed/flexible operation in the region of $E_i > 70$ Wh/m² in Fig. 9b that greater variability would promote. Similarly, for $E_i < 50$ Wh/m² there is no significant resource to be exploited, resulting in low energy conversion. On the other hand, for an optimised flexible operation, signal variability becomes less of an issue. This is indicated by the linear regression relationship between E_i and flexible $E_{0,D,i}$. As the flexible operation makes improved use of the signal variations within each tidal cycle, it counteracts the influence of the overall analysis timeframe signal variability as per Section 4.4. These findings indicate the robustness of flexible operation adds for the tidal range industry.

6. Conclusions

A methodology for the selection of representative periods for tidal range energy assessments at macrotidal sites was presented. Harmonic analysis was utilised to reconstruct tidal elevations around UK’s BODC tide gauge network. Three metrics were tested to facilitate this, namely the Kolmogorov–Smirnov test, the 1-Wasserstein distance and a custom metric that accounts for the magnitude and variability of tidal ranges and energy over prescribed periods. As part of the analysis, a rating score was introduced to evaluate lunar month timeframes within a nodal cycle. We note the following:

- Significant uncertainty arises when comparing tidal characteristics across sites over varying lunar month tidal segments. Indicatively, the significant wave height (i.e. connected to the elevation standard deviation) and the average potential energy within a lunar month can vary by up to 15% and 30% respectively. The variability of tidal range and energy values over a lunar month is greater, exceeding 45%.
- Reconstructed tidal elevation signals are sensitive to the set of constituents used. Taking the UK tide gauge network as an example, a selection of a restricted set of leading constituents (i.e. < 4) can correspond to an averaged deviation from equivalent nodal cycle quantities of 10.5% and 21.2% for significant wave height and potential energy respectively across sites.
- Once sufficient constituents are acknowledged (≥ 8), constrained tide elevation signals correlate well spatially regarding deviations from long-term values. Therefore, once a representative month is identified at one location, the same period can be used with reasonable confidence to compare against multiple sites of the same tidal system. However, studies in the literature have not considered the implications of a specific timeframe selection.

Through this study, we note certain deviations from magnitude and variance of key quantities, which would add a quantifiable bias in design assessments.

- While there is a strong correlation between the available energy resource and the extractable energy from a potential tidal range plant, the latter is highly sensitive to tidal signal variability under a fixed operation schedule. The consideration of an optimised, flexible operation schedule allows the analysis to overcome this sensitivity.
- Representative periods based on either tidal range or the potential energy provide good approximations to the target quantities of interest. Once identified as representative, the same lunar month can be used whether one assesses the response of a tidal power plant to typical tidal range conditions or its energy conversion performance.

Acknowledging harmonic analysis limitations, further work should focus on assessing whether the conclusions of this study are consistent when introducing the uncertainties of regional hydrodynamics models. This becomes valuable when regions of interest depart from tide gauge stations that leverage extensive observation data.

CRedit authorship contribution statement

Konstantinos Pappas: Conceptualisation, Methodology, Formal analysis, Investigation, Writing – original draft. **Lucas Mackie:** Writing – review & editing. **Ilias Zilakos:** Writing – review & editing, Funding acquisition. **Adriaan Hendrik van der Weijde:** Writing – review & editing. **Athanasios Angeloudis:** Conceptualisation, Methodology, Writing – review & editing, Software, Supervision, Funding acquisition.

Declaration of competing interest

The authors declare that they have no known competing financial interests or personal relationships that could have appeared to influence the work reported in this paper.

Acknowledgements

K. Pappas acknowledges the support of Tidetec AS and the EP-SRC WAMESS CDT, United Kingdom (EP/S023801/1). A. Angeloudis acknowledges the support of the NERC Industrial Innovation fellowship grant NE/R013209/2 and the support of the EC H2020 ILIAD DTO project under grant agreement 101037643. All authors thank the anonymous reviewers for their constructive comments throughout the peer-review process.

References

- [1] D. Coles, A. Angeloudis, D. Greaves, G. Hastie, M. Lewis, L. Mackie, J. McNaughton, J. Miles, S. Neill, M. Piggott, D. Risch, B. Scott, C. Sparling, T. Stallard, P. Thies, S. Walker, D. White, R. Willden, B. Williamson, A review of the UK and British Channel Islands practical tidal stream energy resource, *Proc. R. Soc. A* 477 (2255) (2021) 20210469, <http://dx.doi.org/10.1098/rspa.2021.0469>.
- [2] S.P. Neill, A. Angeloudis, P.E. Robins, I. Walkington, S.L. Ward, I. Masters, M.J. Lewis, M. Piano, A. Avdis, M.D. Piggott, G. Aggidis, P. Evans, T.A. Adcock, A. Židonis, R. Ahmadian, R. Falconer, Tidal range energy resource and optimization – Past perspectives and future challenges, *Renew. Energy* 127 (2018) 763–778, <http://dx.doi.org/10.1016/j.renene.2018.05.007>, URL: <https://www.sciencedirect.com/science/article/pii/S0960148118305263>.
- [3] T.A. Adcock, S. Draper, R.H. Willden, C.R. Vogel, The fluid mechanics of tidal stream energy conversion, *Annu. Rev. Fluid Mech.* 53 (1) (2021) 287–310, <http://dx.doi.org/10.1146/annurev-fluid-010719-060207>.
- [4] A. Angeloudis, S.C. Kramer, N. Hawkins, M.D. Piggott, On the potential of linked-basin tidal power plants: An operational and coastal modelling assessment, *Renew. Energy* 155 (2020) 876–888, <http://dx.doi.org/10.1016/j.renene.2020.03.167>, URL: <https://www.sciencedirect.com/science/article/pii/S0960148120305000>.
- [5] C. Jordan, D. Dundovic, A.K. Fragkou, G. Deskos, D.S. Coles, M.D. Piggott, A. Angeloudis, Combining shallow-water and analytical wake models for tidal array micro-siting, *J. Ocean Eng. Mar. Energy* 8 (2) (2022) 193–215.
- [6] M.D. Piggott, S.C. Kramer, S.W. Funke, D.M. Culley, A. Angeloudis, 8.10 - Optimization of marine renewable energy systems, in: T.M. Letcher (Ed.), *Comprehensive Renewable Energy* (Second Edition), second ed., Elsevier, Oxford, 2022, pp. 176–220, <http://dx.doi.org/10.1016/B978-0-12-819727-1.00179-5>, URL: <https://www.sciencedirect.com/science/article/pii/B9780128197271001795>.
- [7] L. Jiang, X. Lu, W. Xu, P. Yao, X. Cheng, Uncertainties associated With Simulating Regional sea surface height and tides: A case study of the East China Seas, *Front. Mar. Sci.* 9 (2022) <http://dx.doi.org/10.3389/fmars.2022.827547>, URL: <https://www.frontiersin.org/articles/10.3389/fmars.2022.827547>.
- [8] F. Harcourt, A. Angeloudis, M.D. Piggott, Utilising the flexible generation potential of tidal range power plants to optimise economic value, *Appl. Energy* 237 (2019) 873–884, <http://dx.doi.org/10.1016/j.apenergy.2018.12.091>, URL: <https://www.sciencedirect.com/science/article/pii/S0306261918319093>.
- [9] R. Burrows, I. Walkington, N. Yates, T. Hedges, J. Wolf, J. Holt, The tidal range energy potential of the West Coast of the United Kingdom, *Appl. Ocean Res.* 31 (4) (2009) 229–238.
- [10] S.D. Hicks, *Understanding Tides*, National Oceanic and Atmospheric Administration, Silver Spring, Maryland, 2006.
- [11] E.P. Kvale, The origin of neap-spring tidal cycles, *Mar. Geol.* 235 (1) (2006) 5–18, <http://dx.doi.org/10.1016/j.margeo.2006.10.001>, URL: <https://www.sciencedirect.com/science/article/pii/S0025322706002544>, Proceedings of the 6th International Congress on Tidal Sedimentology (Tidalites 2004).
- [12] Z. Kowalik, J. Luick, *Modern Theory and Practice of Tidal Analysis and Tidal Power*, Austides Consulting, Eden Hills, South Australia, 2019.
- [13] J. Thiébot, N. Guillou, D. Coles, S. Guillou, On nodal modulations of tidal-stream energy resource in north-western Europe, *Appl. Ocean Res.* 121 (2022) 103091, <http://dx.doi.org/10.1016/j.apor.2022.103091>, URL: <https://www.sciencedirect.com/science/article/pii/S0141118722000451>.
- [14] I.D. Haigh, M. Eliot, C. Pattiaratchi, Global influences of the 18.61 year nodal cycle and 8.85 year cycle of lunar perigee on high tidal levels, *J. Geophys. Res.: Oceans* 116 (C6) (2011) <http://dx.doi.org/10.1029/2010JC006645>, URL: <https://agupubs.onlinelibrary.wiley.com/doi/abs/10.1029/2010JC006645>.
- [15] C.J. Mejia-Olivares, I.D. Haigh, A. Angeloudis, M.J. Lewis, S.P. Neill, Tidal range energy resource assessment of the Gulf of California, Mexico, *Renew. Energy* 155 (2020) 469–483, <http://dx.doi.org/10.1016/j.renene.2020.03.086>, URL: <https://www.sciencedirect.com/science/article/pii/S0960148120304110>.
- [16] A. Cornett, J. Cousineau, I. Nistor, Assessment of hydrodynamic impacts from tidal power lagoons in the Bay of Fundy, *Int. J. Mar. Energy* 1 (2013) 33–54, <http://dx.doi.org/10.1016/j.ijome.2013.05.006>, URL: <https://www.sciencedirect.com/science/article/pii/S2214166913000076>.
- [17] J. Xue, R. Ahmadian, R. Falconer, Optimising the operation of tidal range schemes, *Energies* 12 (2019) 2870, <http://dx.doi.org/10.3390/en12152870>.
- [18] L. Mackie, S.C. Kramer, M.D. Piggott, A. Angeloudis, Assessing impacts of tidal power lagoons of a consistent design, *Ocean Eng.* 240 (2021) 109879, <http://dx.doi.org/10.1016/j.oceaneng.2021.109879>, URL: <https://www.sciencedirect.com/science/article/pii/S0029801821012282>.
- [19] National Tidal and Sea Level Facility, Definitions of tidal levels and other parameters, 2021, National Tidal and Sea Level Facility, NTSLF, URL: <https://www.ntsif.org/tgi/definitions>. (Accessed 10 August 2022).
- [20] G. Aggidis, D. Benzon, Operational optimisation of a tidal barrage across the Mersey Estuary using 0-D modelling, *Ocean Eng.* 66 (2013) 69–81, <http://dx.doi.org/10.1016/j.oceaneng.2013.03.019>, URL: <https://www.sciencedirect.com/science/article/pii/S0029801813001352>.
- [21] G. Aggidis, O. Feather, Tidal range turbines and generation on the Solway Firth, *Renew. Energy* 43 (2012) 9–17, <http://dx.doi.org/10.1016/j.renene.2011.11.045>, URL: <https://www.sciencedirect.com/science/article/pii/S0960148111006471>.
- [22] S. Petley, G. Aggidis, Swansea Bay tidal lagoon annual energy estimation, *Ocean Eng.* 111 (2016) 348–357, <http://dx.doi.org/10.1016/j.oceaneng.2015.11.022>, URL: <https://www.sciencedirect.com/science/article/pii/S0029801815006356>.
- [23] A. Angeloudis, R.A. Falconer, Sensitivity of tidal lagoon and barrage hydrodynamic impacts and energy outputs to operational characteristics, *Renew. Energy* 114 (2017) 337–351, <http://dx.doi.org/10.1016/j.renene.2016.08.033>, URL: <https://www.sciencedirect.com/science/article/pii/S0960148116307340>, Wave and Tidal Resource Characterization.
- [24] A.L. Baker, R.M. Craighead, E.J. Jarvis, H.C. Stenton, A. Angeloudis, L. Mackie, A. Avdis, M.D. Piggott, J. Hill, Modelling the impact of tidal range energy on species communities, *Ocean Coast. Manag.* 193 (2020) 105221, <http://dx.doi.org/10.1016/j.ocecoaman.2020.105221>, URL: <https://www.sciencedirect.com/science/article/pii/S0964569120301319>.
- [25] A. Angeloudis, S.C. Kramer, A. Avdis, M.D. Piggott, Optimising tidal range power plant operation, *Appl. Energy* 212 (2018) 680–690, <http://dx.doi.org/10.1016/j.apenergy.2017.12.052>, URL: <https://www.sciencedirect.com/science/article/pii/S0306261917317671>.
- [26] A. Angeloudis, Tidal range structure operation assessment and optimisation, *Dams Reserv.* 29 (2) (2019) 45–54, <http://dx.doi.org/10.1680/jdare.18.00042>.
- [27] R. Burrows, I. Walkington, J. Holt, J. Wolf, Environmental impacts of tidal power schemes, *Proc. Inst. Civ. Eng.-Marit. Environ.* 162 (2009) 165–177, <http://dx.doi.org/10.1680/maen.2009.162.4.165>.

- [28] L. Mackie, D. Coles, M. Piggott, A. Angeloudis, The potential for tidal range energy systems to provide continuous power: A UK case study, *J. Mar. Sci. Eng.* 8 (10) (2020) <http://dx.doi.org/10.3390/jmse8100780>, URL: <https://www.mdpi.com/2077-1312/8/10/780>.
- [29] J. Xue, R. Ahmadian, O. Jones, Genetic algorithm in tidal range schemes' optimisation, *Energy* 200 (2020) 117496, <http://dx.doi.org/10.1016/j.energy.2020.117496>, URL: <https://www.sciencedirect.com/science/article/pii/S0360544220306034>.
- [30] N. Yates, I. Walkington, R. Burrows, J. Wolf, The energy gains realisable through pumping for tidal range energy schemes, *Renew. Energy* 58 (2013) 79–84, <http://dx.doi.org/10.1016/j.renene.2013.01.039>, URL: <https://www.sciencedirect.com/science/article/pii/S0960148113000773>.
- [31] J. Xia, R.A. Falconer, B. Lin, G. Tan, Estimation of annual energy output from a tidal barrage using two different methods, *Appl. Energy* 93 (2012) 327–336, <http://dx.doi.org/10.1016/j.apenergy.2011.12.049>, URL: <https://www.sciencedirect.com/science/article/pii/S0306261911008452>, (1) Green Energy; (2) Special Section from papers presented at the 2nd International Energy 2030 Conf.
- [32] J. Xia, R.A. Falconer, B. Lin, Hydrodynamic impact of a tidal barrage in the Severn Estuary, UK, *Renew. Energy* 35 (7) (2010) 1455–1468, <http://dx.doi.org/10.1016/j.renene.2009.12.009>, URL: <https://www.sciencedirect.com/science/article/pii/S0960148109005588>, Special Section: IST National Conference 2009.
- [33] S. Bray, R. Ahmadian, R.A. Falconer, Impact of representation of hydraulic structures in modelling a Severn barrage, *Comput. Geosci.* 89 (2016) 96–106, <http://dx.doi.org/10.1016/j.cageo.2016.01.010>, URL: <https://www.sciencedirect.com/science/article/pii/S0098300416300206>.
- [34] J. Zhou, S. Pan, R. Falconer, Effects of open boundary location on the far-field hydrodynamics of a Severn barrage, *Ocean Model.* 73 (2014) 19–29, <http://dx.doi.org/10.1016/j.oceanmod.2013.10.006>.
- [35] N. Čož, R. Ahmadian, R.A. Falconer, Implementation of a full momentum conservative approach in modelling flow through tidal structures, *Water* 11 (9) (2019) <http://dx.doi.org/10.3390/w11091917>, URL: <https://www.mdpi.com/2073-4441/11/9/1917>.
- [36] C. Gao, T.A.A. Adcock, On the tidal resonance of the Bristol Channel, *Int. J. Offshore Polar Eng.* 27 (02) (2017) 177–183, <http://dx.doi.org/10.17736/ijope.2017.as19>.
- [37] D. Idier, F. Paris, G.L. Cozannet, F. Boulahya, F. Dumas, Sea-level rise impacts on the tides of the European Shelf, *Cont. Shelf Res.* 137 (2017) 56–71, <http://dx.doi.org/10.1016/j.csr.2017.01.007>, URL: <https://www.sciencedirect.com/science/article/pii/S0278434317300250>.
- [38] W. Huang, Y. Zhang, Z. Wang, F. Ye, S. Moghimi, E. Myers, H. Yu, Tidal simulation revisited, *Ocean Dyn.* (2022) 1–19, <http://dx.doi.org/10.1007/s10236-022-01498-9>.
- [39] S.B. Lee, M. Li, F. Zhang, Impact of sea level rise on tidal range in Chesapeake and Delaware Bays, *J. Geophys. Res.: Oceans* 122 (5) (2017) 3917–3938, <http://dx.doi.org/10.1002/2016JC012597>, URL: <https://agupubs.onlinelibrary.wiley.com/doi/abs/10.1002/2016JC012597>.
- [40] S. Neill, M. Hemmer, P. Robins, A. Griffiths, A. Furnish, A. Angeloudis, Tidal range resource of Australia, *Renew. Energy* 170 (2021) <http://dx.doi.org/10.1016/j.renene.2021.02.035>.
- [41] Y.H. Park, Analysis of characteristics of Dynamic Tidal Power on the west coast of Korea, *Renew. Sustain. Energy Rev.* 68 (2017) 461–474, <http://dx.doi.org/10.1016/j.rser.2016.10.008>, URL: <https://www.sciencedirect.com/science/article/pii/S136403211630658X>.
- [42] Y.H. Bae, K.O. Kim, B.H. Choi, Lake Sihwa tidal power plant project, *Ocean Eng.* 37 (5) (2010) 454–463, <http://dx.doi.org/10.1016/j.oceaneng.2010.01.015>, URL: <https://www.sciencedirect.com/science/article/pii/S0029801810000235>.
- [43] R. Rtimi, A. Sottolichio, P. Tassi, Hydrodynamics of a hyper-tidal estuary influenced by the world's second largest tidal power station (Rance estuary, France), *Estuar. Coast. Shelf Sci.* 250 (2021) 107143, <http://dx.doi.org/10.1016/j.ecss.2020.107143>, URL: <https://www.sciencedirect.com/science/article/pii/S027277142030874X>.
- [44] B.B. Parker, *Tidal Analysis and Prediction*, National Oceanic and Atmospheric Administration, Silver Spring, Maryland, 2007.
- [45] S. Kramer, Uptide, 2020, URL: <https://github.com/stephankramer/uptide>. (Accessed 19 December 2022).
- [46] BODC, UK tide gauge network. British Oceanographic Data Centre (BODC), 2020, British Oceanographic Data Centre (BODC), BODC URL: <https://www.bodc.ac.uk/>. (Accessed 18 July 2022).
- [47] GEBCO, Gridded Bathymetry Data. General Bathymetry Chart of the Oceans (GEBCO), 2020, General Bathymetry Chart of the Oceans (GEBCO), GEBCO URL: https://www.gebco.net/data_and_products/gridded_bathymetry_data/. (Accessed 19 December 2022).
- [48] Z. Defne, K.A. Haas, H.M. Fritz, Wave power potential along the Atlantic coast of the southeastern USA, *Renew. Energy* 34 (10) (2009) 2197–2205, <http://dx.doi.org/10.1016/j.renene.2009.02.019>, URL: <https://www.sciencedirect.com/science/article/pii/S0960148109000871>.
- [49] A. Angeloudis, L. Mackie, M.D. Piggott, 8.06 - Tidal range energy, in: T.M. Letcher (Ed.), *Comprehensive Renewable Energy (Second Edition)*, second ed., Elsevier, Oxford, 2022, pp. 80–103, <http://dx.doi.org/10.1016/B978-0-12-819727-1.00093-5>, URL: <https://www.sciencedirect.com/science/article/pii/B9780128197271000935>.
- [50] D. Prandle, Simple theory for designing tidal power schemes, *Adv. Water Resour.* 7 (1) (1984) 21–27, [http://dx.doi.org/10.1016/0309-1708\(84\)90026-5](http://dx.doi.org/10.1016/0309-1708(84)90026-5), URL: <https://www.sciencedirect.com/science/article/pii/0309170884900265>.
- [51] R.G. Dean, R.A. Dalrymple, *Water Wave Mechanics for Engineers and Scientists, Vol. 2*, World Scientific Publishing Co. Pte. Ltd., Farrer Road, Singapore, 1991.
- [52] M. Balls, The optimal selection of turbine-generators for tidal power projects and the optimization of their operation, University of Salford, UK, 1988, URL: <http://usir.salford.ac.uk/id/eprint/2041/>, PhD supervisor: Professor E. M. Wilson.
- [53] P.-C. Lin, B. Wu, J. Watada, Kolmogorov-Smirnov two sample test with continuous fuzzy data, in: *Integrated Uncertainty Management and Applications*, Springer Berlin Heidelberg, Berlin, Heidelberg, 2010, pp. 175–186, http://dx.doi.org/10.1007/978-3-642-11960-6_17.
- [54] L. Chen, X. Liu, T. Hu, S. Bao, X. Ye, N. Ma, X. Zhou, Measurement of contagion spatial spread probability in public places: A case study on COVID-19, *Appl. Geogr.* 143 (2022) 102700, <http://dx.doi.org/10.1016/j.apgeog.2022.102700>, URL: <https://www.sciencedirect.com/science/article/pii/S0143622822000716>.
- [55] A. Ramdas, N.G. Trillos, M. Cuturi, On Wasserstein two-sample testing and related families of nonparametric tests, *Entropy* 19 (2) (2017) <http://dx.doi.org/10.3390/e19020047>, URL: <https://www.mdpi.com/1099-4300/19/2/47>.
- [56] D.R. Helsel, R.M. Hirsch, K.R. Ryberg, S.A. Archfield, E. Gilroy, *Statistical Methods in Water Resources: U.S. Geological Survey Techniques and Methods*, Book 4, chapter A3, 458 p., Elsevier Science Ltd., 2020, <http://dx.doi.org/10.3133/tm4a3>.
- [57] C. Spearman, The proof and measurement of association between two things, *Am. J. Psychol.* 15 (1) (1904) 72–101, URL: <http://www.jstor.org/stable/1412159>.
- [58] A. Whitfield, M. Elliott, Ecosystem and Biotic classifications of estuaries and coasts, in: E. Wolanski, D. McLusky (Eds.), *Treatise on Estuarine and Coastal Science*, Academic Press, Waltham, 2011, pp. 99–124, <http://dx.doi.org/10.1016/B978-0-12-374711-2.00108-X>, URL: <https://www.sciencedirect.com/science/article/pii/B978012374711200108X>.
- [59] M. Lewis, A. Angeloudis, P. Robins, P. Evans, S. Neill, Influence of storm surge on tidal range energy, *Energy* 122 (2017) 25–36, <http://dx.doi.org/10.1016/j.energy.2017.01.068>.
- [60] Q. Ma, T. Adcock, Modification of tidal resonance in the Severn Estuary by a barrage and lagoon, *J. Ocean Eng. Mar. Energy* 6 (2020) <http://dx.doi.org/10.1007/s40722-020-00166-8>.
- [61] N. Hanousek, R. Ahmadian, Assessing the sensitivity of tidal range energy models to water level accuracy, in: *Proceeding of the 39th IAHR World Congress*, 2022.